LA-9527-MS

c.3

Los Alamos National Laboratory is operated by the University of California for the United States Department of Energy under contract W-7405-ENG-36.

# *Jet Penetration of Inerts and Explosives*

Los Alamos Los Alamos National Laboratory
Los Alamos, New Mexico 87545

Prepared by Louise Criss, Group T-14

LA-9527-MS

UC-45
Issued: November 1982

# Jet Penetration of Inerts and Explosives

Charles L. Mader
George H. Pimbley
Allen L. Bowman

Los Alamos
Los Alamos National Laboratory
Los Alamos, New Mexico 87545

# JET PENETRATION OF INERTS AND EXPLOSIVES

by

Charles L. Mader, George H. Pimbley, and Allen L. Bowman

## ABSTRACT

The two-dimensional Eulerian hydrodynamic code 2DE, with the shock initiation of heterogeneous explosive burn model called Forest Fire, is used to model numerically the interaction of jets of steel or tantalum with steel, water, and explosive targets.

The calculated jet velocity relative to the penetration velocity into inert targets is a function of the square root of the target density divided by the jet density.

The calculated penetration velocities into explosives, initiated by a low-velocity jet, are significantly less than for inerts of the same density. The detonation products near the jet tip have a higher pressure than that of nonreactive explosives, and thus slow the jet penetration. At high jet velocities, the calculated penetration velocities are similar for reactive and inert targets.

---

## I. INTRODUCTION

The initiation of propagating detonations in PBX 9404 and PBX 9502 by copper, aluminum, and water jets was modeled numerically in Ref. 1, using the two-dimensional Eulerian hydrodynamic code 2DE.[2]

Studies of shock initiation by jets near the critical conditions contrast with other shock initiation studies in that, for the latter, if detonation occurred, it was because the initiating shock wave was of sufficient strength and duration to build up to detonation. The propagating detonation was assured by the large geometry. In near-critical jet initiation, however, a prompt detonation of the explosive results, which builds to a propagating detonation only if the shock wave produced by the jet is of sufficient magnitude and duration.

The penetration velocities of projectiles interacting with explosives initiated by the projectile are reported[3] to be much lower than the penetration velocities of inerts of the same density. This study examined projectile penetration dynamics in inert and reactive targets. Because jets formed by a shaped charge with a metal cone contain small-diameter, high-velocity projectiles, the jets can be approximated by cylinders or balls of uniform velocity with the appropriate dimensions.

The classic paper on jet formation and penetration by Birkhoff, MacDougall, Pugh, and Taylor[4] describes what is called the "ideal" penetration velocity. If we assume Bernoulli's theorem applies (that is, that the jet pressure is large compared to the target or jet material strengths and that pressure is the same in the jet and target near the interface), then

$$0.5\ \rho_j (V_j - V_p)^2 = 0.5\ \rho_t V_p^2 \quad ,$$

where $\rho$ is density, V is velocity, j implies jet, t implies target, and p signifies penetration.

We rearrange the expression to find the ratio of the jet velocity to jet penetration velocity,

$$\frac{V_j}{V_p} = 1 + \sqrt{\rho_t/\rho_j} \quad .$$

We use this expression to determine the penetration velocity for a 1.0-cm/μs steel jet interacting with various targets, as follows.

| Target | Penetration Velocity (cm/μs) |
|---|---|
| Steel | 0.5 |
| Aluminum | 0.628 |
| Comp B | 0.682 |
| Water | 0.738 |

Bernoulli's theorem is for steady motion of an incompressible uniform fluid. For a compressible fluid, the ideal penetration velocity expression is exact only for a constant density system; however, the experimental penetration data from many studies of inert jets penetrating inerts are adequately described using the ideal model.

The penetrations of an aluminum target by an aluminum jet and of a steel target by a steel jet were modeled using the particle-in-cell technique by Harlow and Pracht.[5] They concluded that their calculated penetration velocities approached the ideal values.

Copper jet penetration into an aluminum target was calculated by Johnson[6] using his two- and three-dimensional Eulerian hydrodynamic codes. His calculated penetration velocity agrees with the ideal values.

The penetration velocity of a 13-mm-diam steel ball moving at various velocities and impacting a 25-mm-thick cylinder of PBX 9404 or Composition B was reported by Rice.[3] The data were generated at Ballistic Research Laboratory by R. Frey. Experimental data and Eulerian calculations by Rice indicated that the penetration velocity was markedly decreased, beyond the critical projectile velocity for initiation of detonation, and was significantly less than predicted by the ideal model.

This study examined the jet penetration of inerts and explosives by comparing calculated and experimental projectile penetrations to determine the nature of the process and the cause of the observed failure of the ideal penetration model for explosives.

## II. STEEL JET PENETRATING STEEL

Two PHERMEX radiographs of a steel jet penetrating a steel block have been published.[7] The steel jet was formed by a 4.0-mm-thick hemishell driven by a 60.0-mm-thick PBX-9404 hemisphere. The jet interacted with a steel block after 308 mm of free run from the center of the steel hemisphere.

The jet tip velocity was 18 mm/μs and the jet velocity decreased approximately 1.3 mm/μs for each 10 mm of jet length. Radiograph 1185 was taken after the jet had penetrated 45 mm of steel in 6 μs with an average penetration velocity of 7.5 mm/μs. Radiograph 1181 was taken after the jet had penetrated an additional 35 mm of steel in 7.0 μs with an average penetration velocity of 5.0 mm/μs. The jet velocity decays from 18 mm/μs to 10 mm/μs after a run of 24 ft in the air. The jet diameter is uncertain because of its diffuse boundaries in the radiograph. The jet diameter increases and the jet interface is more diffuse along the length of the jet. We therefore examined 8- and 12-mm-diam jets in our models.

The radiographs are shown in Figs. 1 and 2. Calculated density profiles, with the experimental shock front and interface, are shown in Figs. 3 and 4.

The 2DE computer code described in Ref. 2 was used to model the flow. Equation-of-state parameters used for 347 stainless steel are the same as given in Appendix B of Ref. 8.

The steel shock Hugoniot was described by $U_s = 4.58 + 1.51\ U_p$, where $U_s$ is shock velocity and $U_p$ is particle velocity. The initial density of the steel was 7.917 mg/mm$^3$ and the Grüneisen gamma was 1.25. Elastic-plastic terms were negligible, and tension was permitted only in the target.

The calculated profiles are sensitive to the jet description. The jet initially has steel's standard density, but the velocity gradient results in the jet density decreasing with time.

The calculated pressures, densities, and vertical velocities near and parallel to the vertical z-axis are shown in Fig. 5 at various times. Pressure and velocity at the interface between the steel target and the advancing jet tip are shown as functions of time in Fig. 6. Contours of pressure, energy, and velocity in R and Z directions are shown in Fig. 7 at 6.0 µs and in Fig. 8 at 13.0 µs.

The experimentally observed steel jet penetration into a steel plate appears to be adequately reproduced, considering the complicated nature of the jet. The hole observed between the jet and target walls also appears to be substantially reproduced. The jet material appears primarily along the side of the hole made in the target and in the splash wave. Reference 4 states that "careful weighings have shown that a metal jet is captured by a metal target, which loses no weight except a very small amount at the front surface." Mautz has reported that high-velocity steel jets penetrating steel remain partly on the target, and partly leave the target in a vapor or liquid form.

The observed agreement between the radiographs and numerical model suggests that the important features of jet penetration are described by the fluid dynamics of the process. To examine the problem further, we simplify our jet to a rod or sphere, initially moving with a uniform velocity.

## III. STEEL ROD PENETRATING STEEL

Having demonstrated that steel target penetration by a steel jet of decreasing velocity can be modeled numerically, we next examine the penetration physics of a simple system.

A 10-mm-diam steel rod with a 15-mm/µs velocity was modeled similarly to the steel jet model described in Sec. II. The mesh cells were 1-mm square and the time step was $4 \times 10^{-3}$ μs. The system was described by 50 cells in the radial direction and 100 cells along the z-axis.

The calculated pressures, densities, and vertical velocities along and near the vertical z-axis are shown in Fig. 9 at various times. Pressure and velocity at the interface between the steel target and the upper tip of the rod are shown as functions of time in Fig. 10. Contours of pressure, density, energy, and velocity in R and Z directions are shown in Fig. 11 at 4.0 μs and in Fig. 12 at 8.0 μs.

The steel rod sends an initial shock pressure of about 950 GPa into the steel target at a 16-mm/μs shock velocity and a 7.5-mm/μs particle velocity. Radial motion of the steel target, and side rarefactions, decreased the interface pressure to about 250 GPa, and the particle velocity remained at about 7.5 mm/μs. A diverging, approximately steady state profile developed near the jet-target interface, which continued until the rod length was consumed. The shock wave was supported by the higher pressure at the rod-target interface.

A steel rod of the same dimensions but with an initial velocity of 10 mm/μs was modeled also.

The calculated pressures, densities, and vertical velocities along and near the vertical z-axis are shown in Fig. 13 at various times. Pressure and velocity at the interface between the steel target and the upper tip of the rod are shown as functions of time in Fig. 14.

The steel rod sent an initial shock pressure of about 480 GPa into the steel target, along with a 12.1-mm/μs shock velocity and a 5.0-mm/μs particle velocity. The radial motion decreased the interface pressure to 100 GPa; the particle velocity remained near 5.0 mm/μs for 18 μs, or a penetration distance of 90 mm. A shock wave in the target, with pressure less than one-third of the interface pressure, was supported by a 100-GPa pressure at the target-rod interface.

The penetration velocity quickly approached the "ideal" penetration velocity (half the initial rod velocity) for a steel rod entering a steel target.

The initial high-pressure shock wave formed at the rod-target interface was quickly degraded by side rarefactions and divergence to the "ideal" interface pressure, P, of $\frac{1}{2}\rho V_p^2$, whereas the particle velocity remained unchanged, as expected for jets and targets of the same material. The shock impedance relationship may be expressed as $V_j/V_p = 1 + \rho_t U_{st}/\rho_j U_{sj}$, where $U_{st}$ is the shock velocity and $P = \rho_t U_s V_p$. For jets and targets of the same material, $V_p = 0.5\ V_j$ for both the initial shock match across the interface and for the later penetration after steady state is achieved; the pressure decreased from $\rho_t U_{st} V_p$ to $\frac{1}{2}\rho V_p^2$. The high pressure near the rod-target interface supported a lower pressure shock wave that moved out into the target ahead of the rod-target interface with a shock speed similar to the penetration velocity of the rod.

## IV. TANTALUM ROD PENETRATION

To examine the effect of different materials on the penetration process, we modeled an unreported experiment performed by Campbell and Hantel at the Los Alamos National Laboratory. They determined that, with an initial velocity of 7.3 to 6.6 mm/μs, the penetration velocity of a tantalum jet into a steel plate was 4.0 mm/μs. The tantalum shock Hugoniot was described by $U_s = 3.414 + 1.201 U_p$, $\rho = 16.69$ mg/mm$^3$, and $\gamma = 1.4$.

In Table I, the calculated penetration velocity of the tantalum rod is 4.0-mm/μs for a 7.3-mm/μs rod, and 3.7 mm/μs for a 6.6-mm/μs rod. The 4.0-mm/μs experimental penetration velocity, for a jet with a velocity between 7.3 and 6.6 mm/μs, is well reproduced by the calculations.

The good agreement between experiment and calculation for the tantalum jet penetrating steel suggests that we can use the model to examine other systems.

TABLE I

CALCULATED AND IDEAL MODEL PRESSURES AND VELOCITIES[a]

| System | Initial Rod Velocity | Initial Shock Pressure | Initial Particle Velocity | Penetration Velocity Calc. Final | Penetration Velocity Ideal | Interface Pressure Calc. Final | Interface Pressure Ideal |
|---|---|---|---|---|---|---|---|
| Tantalum rod penetrating steel | 7.3 | 370 | 4.2 | 4.0 | 4.33 | 80 | 74 |
| Tantalum rod penetrating steel | 6.6 | 310 | 3.8 | 3.7 | 3.91 | 60 | 60 |
| Tantalum rod penetrating water | 6.4 | 68 | 5.5 | 5.2 | 5.14 | 13 | 13.2 |
| Tantalum rod penetrating inert Composition B | 6.4 | 110 | 5.0 | 4.6 | 4.85 | 20 | 20.1 |
| Tantalum rod penetrating inert Composition B | 2.0 | 17 | 1.7 | 1.64 | 1.51 | 2 | 1.97 |
| Tantalum rod penetrating reactive Composition B | 2.0 | 30 | 1.8 | 1.37 | 1.51 | 6 | 1.97 |

---

[a] Pressures are in gigapascals, and velocities are in millimeters per microsecond.

As predicted by the ideal model, the tantalum ($\rho = 16.69\ mg/mm^3$) rod at the same initial velocity penetrates inert Composition B ($\rho = 1.715\ mg/mm^3$) faster than steel, and penetrates water ($\rho = 1.0\ mg/mm^3$) even faster. The ideal model interface pressures and penetration velocities agree well with the numerical results over a wide range of velocities and densities, except for the reactive Composition B, where the interface pressure is three times greater in the calculation than in the ideal.

The pressure, density, and velocity in the R and Z directions are shown in Fig. 15 for the tantalum rod with a 6.4-mm/μs initial velocity penetrating steel, and in Fig. 16 for the tantalum rod penetrating water. A larger tip diameter develops on the tantalum rod and makes a larger hole in the steel target than in the water target. Pressure and velocity at the interface between the upper tip of the advancing tantalum rod and the steel target are shown in Fig. 17, and between the tantalum tip and the water target in Fig. 18. The pressure and velocity one-dimensional graphs along the tantalum rod (with a 2.0-mm/μs initial velocity), and on into the Composition B target, are shown in Fig. 19 for the unreacted and detonated Composition B after 6.0 μs. The tantalum rod interface pressures are larger and the interface velocities are lower for the reactive case.

We examine the reactive case in detail in the next section.

## V. STEEL BALL PENETRATION OF EXPLOSIVES

Rice reported[3] the penetration velocity of a steel ball, 13 mm in diameter, moving at varying speeds and striking 25-mm-thick cylinders of either PBX 9404 or Composition B.

We have modeled this system numerically, and we compared the results with the experimental data of Frey. The Forest Fire[2] description of heterogeneous shock initiation described the explosive burn. The HOM equation of state, and Forest Fire rate constants for PBX 9404 and Composition B, were identical to those described in Ref. 2. The mesh was 0.5416 mm by 0.5 mm and the time step was 0.005 μs. The computational problem was 78 cells in height and 20 cells in width.

Figure 20 shows the experimental data and the calculated results of steel ball interaction with PBX 9404 or Composition B. The ball velocity loss is defined as the initial ball velocity less the penetration velocity. The agreement demonstrates that the model describes the important processes of explosive penetration.

When the steel ball was penetrating inert or nearly inert explosive, the penetration velocity could be described by the ideal model. When the ball velocity was just sufficient to cause propagating detonation, however, the observed and calculated penetration velocities were much less than predicted by the ideal model. As the ball velocity was increased, the difference between the actual and ideal penetration velocities decreased. A summary of the ball penetration calculations is given in Table II.

TABLE II

BALL PENETRATION CALCULATIONS

| | Velocity (mm/μs) | State | Velocity Loss (mm/μs) | $V_p$ (mm/μs) | $V_p$ Ideal[a] | $V_{loss}$ Ideal (mm/μs) |
|---|---|---|---|---|---|---|
| Steel/Composition B | 2.2 | Reacted | 1.0 | 1.2 | 1.5 | 0.7 |
| | 2.0 | Late reaction | >0.8 | 1.2 | 1.365 | 0.64 |
| | 1.7 | No reaction | 0.5 | 1.2 | 1.16 | 0.54 |
| | 1.0 | No reaction | 0.25 | 0.75 | 0.68 | 0.32 |
| | 0.5 | No reaction | 0.10 | 0.40 | 0.34 | 0.16 |
| | 1.5 | No reaction | 0.30 | 1.2 | 1.02 | 0.477 |
| | 3.0 | Reacted | 1.2 | 1.8 | 2.047 | 0.953 |
| | 2.0 | No reaction permitted | 0.5 | 1.5 | 1.365 | 0.635 |
| | 3.0 | No reaction permitted | 0.80 | 2.25 | 2.047 | 0.953 |
| Steel/PBX 9404 | 1.4 | Reacted | 0.80 | 0.60 | 0.944 | 0.456 |
| | 1.2 | Late reaction | >0.75 | 0.45 | 0.81 | 0.39 |
| | 1.0 | No reaction | 0.35 | 0.65 | 0.675 | 0.325 |
| | 0.5 | No reaction | 0.15 | 0.35 | 0.337 | 0.163 |

---

[a] $V_p$ ideal for Composition B is 0.682 (ball velocity).
$V_p$ ideal for PBX 9404 is 0.674 (ball velocity).

A plot of the interface pressure and velocity in the Z direction near the z-axis, as functions of time, for 1.0- and 1.2-mm/μs balls interacting with PBX 9404 is shown in Fig. 21. The contours and one-dimensional graphs are shown in Figs. 22 and 23. The 1.2-mm/μs ball results in prompt initiation of the PBX 9404, and the interface pressure is much higher and velocity loss greater than for the 1.0-mm/μs ball (which does not cause prompt initiation).

In Ref. 1 we showed that the Held experimental critical condition for propagating detonation--the jet velocity squared times the jet diameter ($V_j^2d$)--adequately described the experimental and theoretical results. The steel ball must present an "effective diameter" to the explosive. The critical ball velocity for PBX 9404 shown in Fig. 20 is 1.14 mm/μs. The $V_j^2d$ for PBX 9404, reported in Ref. 1, is 16.0; therefore, the ball has an effective diameter of 12.3 mm. This is, within the calibration error, not significantly different from the actual ball diameter of 13.0 mm. The critical ball velocity for Composition B, shown in Fig. 20, is 1.8 mm/μs. The $V_j^2d$ for Composition B, reported in Ref. 1, is 29; therefore, the ball has an effective diameter of 9.0 mm when shocking Composition B.

Because the steel ball exhibits a complicated flow, we examined a simpler system to demonstrate the essential features of the flow.

The ball was replaced by a steel rod of the same diameter, and rods with velocities of 2.0 and 6.0 mm/μs were calculated interacting with reactive and nonreactive Composition B. The interface pressures and velocities near the advancing upper tip of the steel rod, as functions of time, are shown in Figs. 24 and 25. A summary of the rod calculation is given in Table III.

The lowered penetration velocity of a projectile moving into detonating (rather than nondetonating or inert) explosives is caused by the higher pressure at the projectile-detonation product interface. The ideal model assumes that the pressure at zero particle velocity is zero, which is correct for inerts; however, for explosives the constant volume detonation pressure at zero particle velocity is approximately 10 GPa for a slab of Composition B. In diverging flow, the detonation product pressure at zero particle velocity is about 5 GPa. The effect is not included in the ideal model, so it fails to account for the velocity decrease.

If we assume that the ideal model is appropriate for the steel rod, and if we set the calculated detonation product interface pressure, 5.0 GPa for the

## TABLE III

## STEEL ROD PENETRATING COMPOSITION B[a]

| Condition | Initial Rod Velocity[b] | Penetration Velocity[b] | | Interface Pressure[b] | |
|---|---|---|---|---|---|
| | | Calc. Final | Ideal | Calc. Final | Ideal |
| Reactive | 6.0 | 4.0 | 4.09 | 18.0 | 14.4 |
| Reactive | 2.0 | 1.0 | 1.365 | 5.0 | 1.59 |
| Inert | 6.0 | 4.0 | 4.09 | 15.0 | 14.4 |
| Inert | 2.0 | 1.4 | 1.365 | ~1.5 | 1.59 |

---

[a] Ideal penetration velocity is 0.682 (rod velocity) and ideal interface pressure is 0.8575 (penetration velocity)$^2$.

[b] Velocities are in millimeters per microsecond and pressures are in gigapascals.

2.0-mm/μs rod, equal to $[\frac{1}{2}\rho_j(V_j - V_p)^2]$, we estimate a 0.9-mm/μs penetration velocity. This is close to the 1.0 mm/μs calculated.

The relative difference between the ideal penetration velocity and the calculated penetration velocity decreases with increasing projectile velocity; the ideal model becomes better at higher projectile velocities, where the difference between the explosive reactive and nonreactive pressures (of about 4 GPa) becomes insignificant. In the next section we shall examine the effect of projectile velocity on the penetration velocity in more detail.

## VI. STEEL ROD PENETRATION OF PBX 9404

We have modeled a 16-mm-diam steel rod moving at velocities lower than those necessary for initiating propagating detonation (1.0 mm/μs) in PBX 9404, and at velocities great enough to penetrate the explosive faster than the detonation velocity (8.8 mm/μs). The study investigated the penetration velocity in explosives throughout the range of possible jet velocities and examined the steel rod and explosive interface pressure effect described in the previous section. It also determined what would occur if the penetration velocity were greater than the C-J detonation velocity.

The Forest Fire rate constants and the HOM equation of state used for PBX 9404 were described in Ref. 2. The mesh was 2.0-mm by 2.0-mm square. The problem was described by 25 cells in the radial direction and 65 cells in the axial direction. The rod was 10 cells long and the steel target was 55 cells high. The time step for the calculation was 0.008 μs.

A summary of the results of the calculations is given in Table IV.

The interface or rod tip pressures and velocities as functions of time, for a steel rod with a 15-mm/μs initial velocity penetrating PBX 9404, are shown in Fig. 26. The contours and one-dimensional graphs are shown in Fig. 27. The steel rod penetrates the PBX 9404 at 10.6 mm/μs, and it forms a steady overdriven detonation wave moving at the same velocity as the steel rod, and with an overdriven effective C-J pressure of 100 GPa. The C-J pressure of PBX 9404 is 36.5 GPa and the C-J velocity is 8.8 mm/μs. The calculation demonstrates that highvelocity jets cannot be used to destroy an explosive charge without initiating an overdriven propagating detonation.

When the rod penetration velocity becomes less than the C-J detonation velocity, the detonation wave moves away from the rod surface. To illustrate

TABLE IV

STEEL ROD PENETRATING PBX 9404

| Initial Rod Velocity (mm/μs) | Final Calc. Penetration Velocity (mm/μs) | Ideal Penetration Velocity[a] (mm/μs) | Interface Pressure (GPa) | Ideal Interface Pressure[b] (GPa) | Diverging Effective C-J Pressure (GPa) | Detonation Velocity (mm/μs) | Comments |
|---|---|---|---|---|---|---|---|
| 15.0 | 10.6 | 10.117 | 100 | 94.37 | 90 | 10 | Steady overdriven detonation wave |
| 13.0 | 9.2 | 8.768 | 75 | 70.89 | 60 | 8.8 | Steady overdriven detonation wave |
| 11.0 | 7.8 | 7.419 | 55 | 50.75 | 40 | 8.8 | Decaying wave moving faster than rod |
| 9.0 | 6.2 | 6.07 | 38 | 33.97 | 36 | 8.7 | Diverging detonation wave moving faster than rod |
| 8.0 | 5.5 | 5.396 | 31 | 26.84 | 35 | 8.7 | Diverging detonation wave moving faster than rod |
| 5.0 | 3.2 | 3.37 | 15 | 10.5 | 35 | 8.7 | Diverging detonation wave moving faster than rod |
| 3.0 | 1.8 | 2.02 | 8 | 3.77 | 35 | 8.7 | Diverging detonation wave moving faster than rod |
| 2.5 | 1.4 | 1.686 | 7 | 2.6 | 35 | 8.7 | Diverging detonation wave moving faster than rod |
| 2.0 | 1.1 | 1.35 | 6 | 1.7 | 35 | 8.7 | Diverging detonation wave moving faster than rod |
| 1.5 | 0.6 | 1.01 | 5 | 0.9 | 35 | 8.7 | Diverging detonation wave moving faster than rod |
| 1.0 | 0.25 | 0.67 | 5 | 0.4 | 35 | 8.7 | Diverging detonation wave moving faster than rod |
| 0.7 | 0.5 | 0.47 | 0 | 0.2 | -- | ---- | No detonation, decaying shock wave |
| 0.5 | 0.36 | 0.34 | 0 | 0.1 | -- | ---- | No detonation, decaying shock wave |
| 0.3 | 0.22 | 0.20 | 0 | 0.04 | -- | ---- | No detonation, decaying shock wave |

---

[a] 0.674 rod velocity.

[b] 0.922 (penetration velocity)$^2$.

this, Fig. 28 shows the interface or rod tip pressure and velocities as functions of time for a steel rod with a 5-mm/μs initial velocity penetrating PBX 9404. Contours and one-dimensional graphs along the vertical z-axis are shown in Fig. 29. The steel rod penetrates the PBX 9404 at 3.2 mm/μs. The detonation wave proceeds at 8.7 mm/μs with a diverging effective C-J pressure of 35 GPa. The interface detonation product pressure is 15 GPa, which is 4.5 GPa greater than the ideal interface pressure at the rod tip of 10.5 GPa. As discussed in the previous section, the ideal model assumes that the pressure at zero particle velocity is zero, which is incorrect for constant volume detonation. A slower penetration velocity results than that expected from the ideal model.

The effect of the 4-GPa additional interface pressure is most apparent when the rod velocity just suffices to cause prompt propagating detonation. To il-illustrate this, Fig. 30 shows the velocity as a function of time for a steel rod with a 1.5-mm/μs initial velocity penetrating PBX 9404. Contours and one-dimensional graphs are shown in Fig. 31. The steel rod penetrates the PBX 9404 at 0.6 mm/μs, which is 0.4 mm/μs slower than it would penetrate the PBX 9404 if it were inert. The steel rod interface pressure is 5.0 GPa, which is 4 GPa higher than the 0.9-GPa ideal interface pressure. Illustrating the importance of this increased interface pressure upon penetration velocity, the calculated penetration velocity is about the same for the 0.7-mm/μs steel rod, where the explosive does not decompose, as for the 1.5-mm/μs rod, where the explosive detonates.

## VII. CONCLUSIONS

For engineering purposes, the initial jet penetration velocity into an inert can be estimated, using the shock-matching relationship,

$$\frac{V_j}{V_p} = 1 + \frac{\rho_t U_{st}}{\rho_j U_{sj}} \quad .$$

Here, $V_j$ is initial jet velocity, $V_p$ is penetration velocity, $\rho$ is density, $U_s$ is shock velocity, j implies jet, and t signifies target. The initial shock pressure can be estimated using $P = \rho_t U_{st} V_p$. Final penetration velocity can be estimated, using Bernoulli's theorem, from

$$\frac{V_j}{V_p} = 1 + \sqrt{\frac{\rho_t}{\rho_j}} \quad .$$

The interface pressure, P, at the jet tip can be estimated using

$$P = 0.5\ \rho_t V_p^2 \quad .$$

When using a high explosive as the target, the pressure expression needs an additional term, p*, and the Bernoulli equation for explosives becomes

$$0.5\ \rho_j (V_j - V_p)^2 = 0.5\ \rho_t V_p^2 + p^* \quad ,$$

where we have determined p* to be approximately 4.0 GPa for the explosives studied.

Obviously, these are only approximations and a more reliable estimate can be obtained using the numerical methods described in this report. If the jet velocity decreases significantly or the projectile length is not much longer than the projectile diameter, numerical calculations are necessary.

Even if the jet particle or projectile is no longer than the diameter, the critical velocity for initiating propagating detonation can be estimated using the projectile diameter and the Held critical $V^2d$ expression discussed in this report and Ref. 1.

A jet with a penetration velocity greater than the C-J detonation velocity of an explosive results in an overdriven detonation wave proceeding ahead of the jet at a velocity near that of the jet.

The calculated penetration velocity into explosives that are initiated by a low-velocity jet is significantly less than for inerts of the same density. Detonation products near the jet tip have a higher pressure than in inert materials of the same density, and thus slow the jet penetration more. The effect is less important as the jet velocities increase.

Most significantly, if the jet diameter and velocity histories are known, all the experimentally observed jet penetration behavior of metals or explosives can be modeled numerically. Also, if the jet or projectile length is known, the penetration depth and hole diameter may be calculated.

## ACKNOWLEDGMENTS

The authors gratefully acknowledge the contributions of James N. Johnson, who explained why the initial shock particle velocity was identical to the penetration velocity for targets and jets of the same material. They also acknowledge the suggestions, contributions, and encouragement of L. W. Hantel, A. W. Campbell, C. W. Mautz, D. L. Upham, and S. D. Gardner of the Los Alamos National Laboratory; N. E. Hoskin, AWRE; and Peter R. Lee, RARDE.

## REFERENCES

1. Charles L. Mader and George H. Pimbley, "Jet Initiation of Explosives," Los Alamos Scientific Laboratory report LA-8647 (February 1981).
2. Charles L. Mader, Numerical Modeling of Detonations (University of California Press, Berkeley, 1979).
3. M. H. Rice, "Penetration of High Explosives by Inert Projectiles," Systems, Science and Software report SS-R-78-3512 (1977).
4. Garrett Birkhoff, Duncan P. MacDougall, Emerson M. Pugh, and Sir Geoffrey Taylor, "Explosives with Lined Cavities," J. App. Phys. 19, 563-582 (1948).
5. Francis H. Harlow and William E. Pracht, "Formation and Penetration of High-Speed Collapse Jets," Phys. Fluids 9, 1951-1959 (1966).
6. Wallace E. Johnson, "Three-Dimensional Computations in Penetrator-Target Interactions," Ballistic Research Laboratory report BRL CR 338 (1977).
7. Charles L. Mader, LASL PHERMEX Data, Vol. III (University of California Press, Berkeley, 1980).
8. Charles L. Mader and Milton Samuel Shaw, "User's Manual for SIN," Los Alamos Scientific Laboratory report LA-7264-M (September 1978).

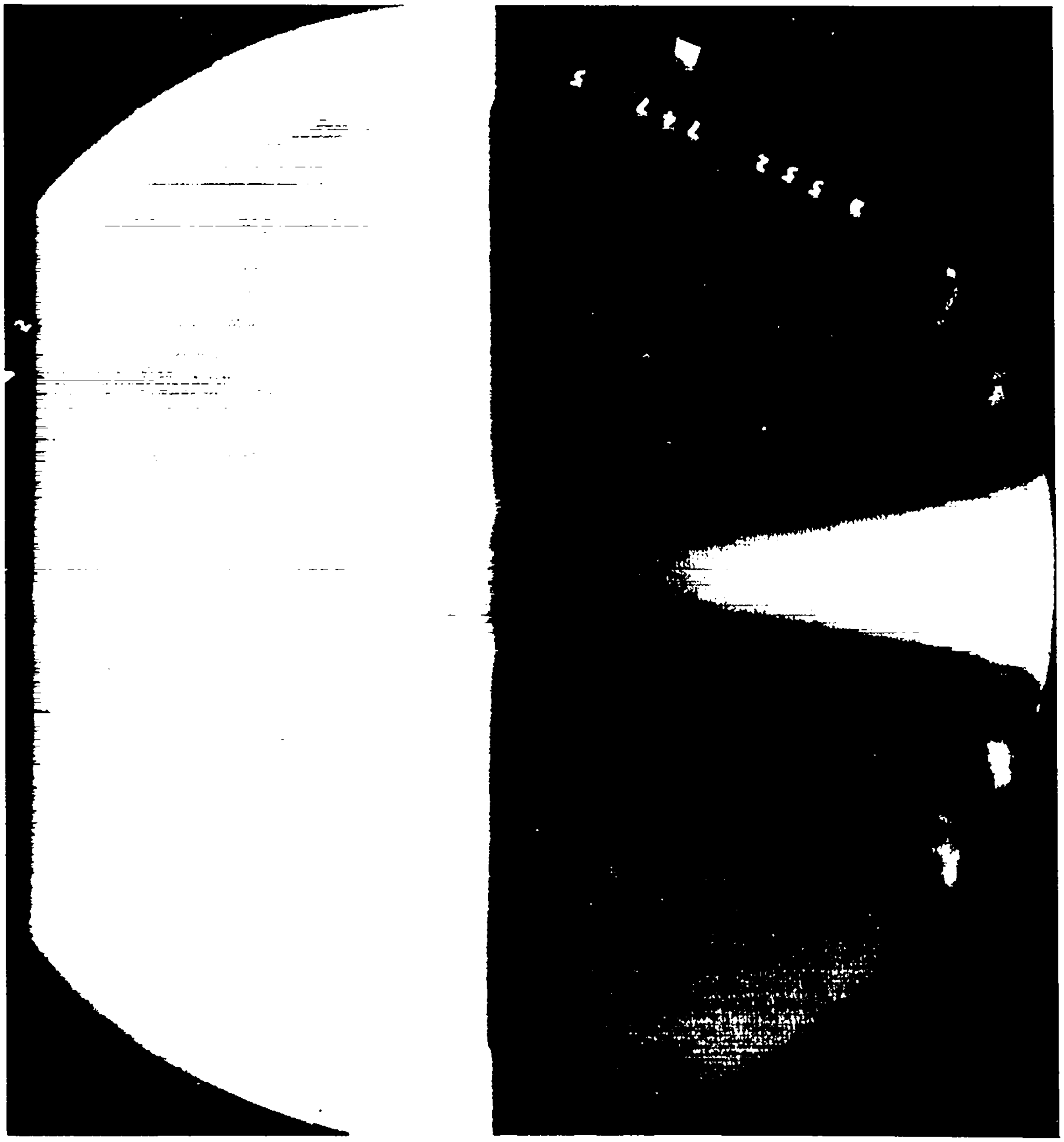

Fig. 1.
Shot 1185. A steel jet formed by a 4.0-mm-thick steel hemishell, which was driven by a 60.0-mm-thick PBX-9404 hemisphere, penetrated a 304 stainless steel block. The jet traveled for 35.57 μs. The steel block was 308 mm from the center of the steel hemishell. The radiographic time was 79.02 μs.

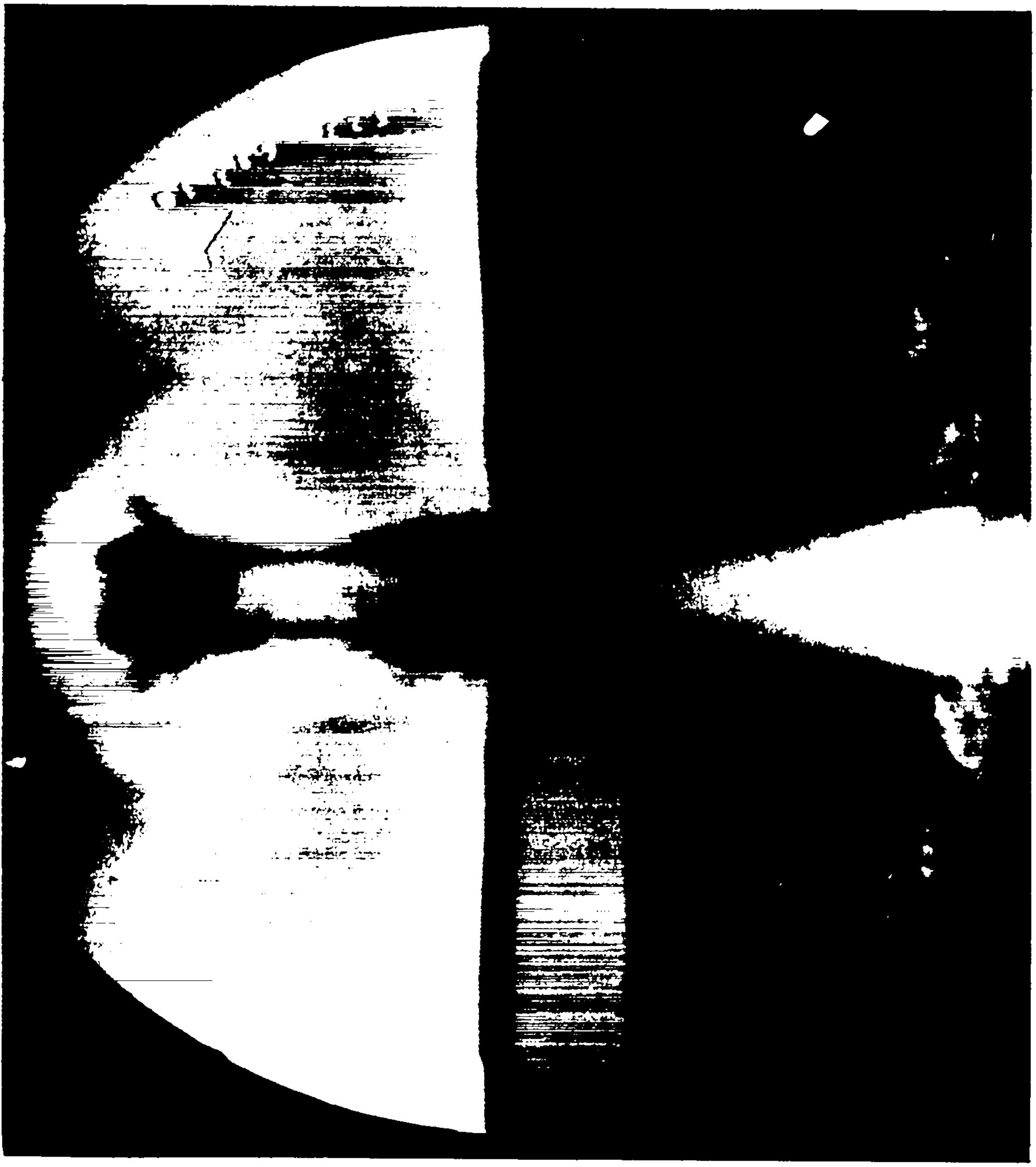

Fig. 2.

Shot 1181. A 304 stainless steel block was penetrated by a steel jet formed by a 4.0-mm-thick steel hemishell driven by a 60.0-mm-thick PBX-9404 hemisphere. The jet traveled for 42.53 μs. The steel block was 308 mm from the center of the steel hemishell. The radiographic time was 85.99 μs.

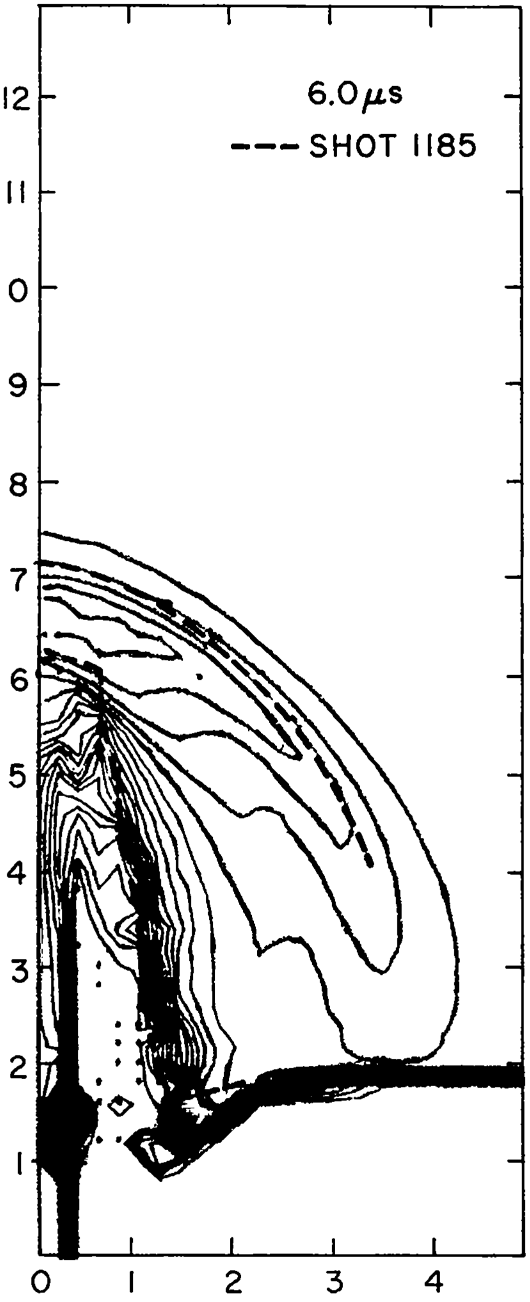

Fig. 3.
Calculated density profiles, after 6.0 μs of penetration, of a steel block 110 mm long and 50 mm wide, by an 8.0-mm-thick steel jet moving with a tip velocity that has decreased to 12 mm/μs. The experimental shock front profile and target interface are shown for shot 1185. The jet has penetrated 45 mm of steel. The density contour interval is 0.5 mg/mm$^3$.

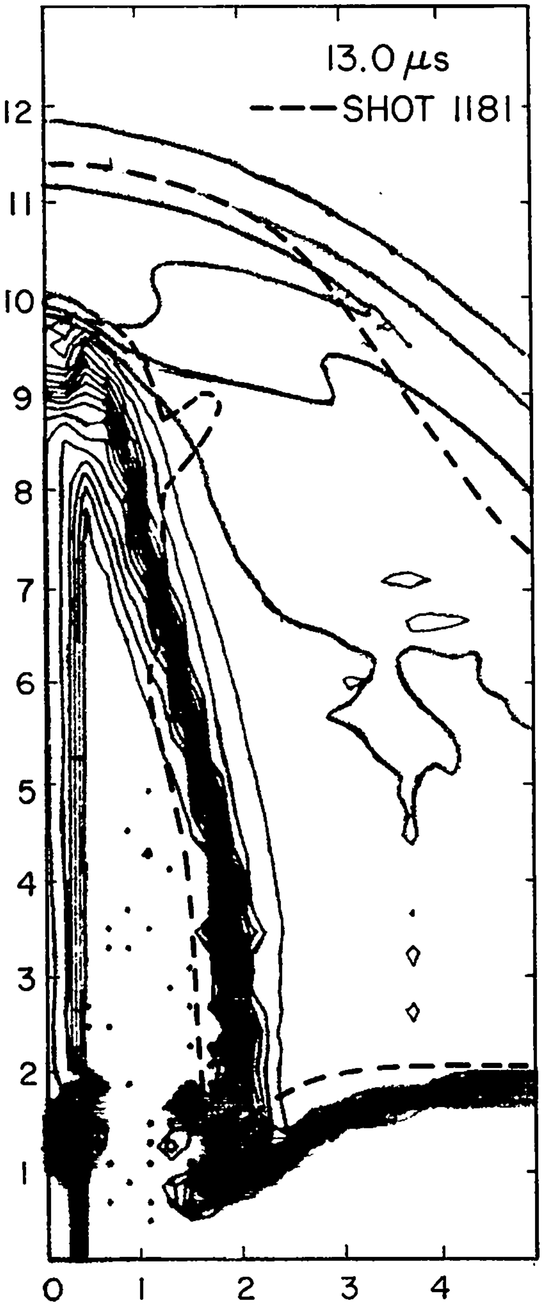

Fig. 4.
Calculated density profiles after 13 μs of penetration of a steel block 110 mm long by 50 mm wide, by an 8.0-mm-thick steel jet moving with tip velocity that has decreased to 7.75 mm/μs. The experimental shock front profile and target interface are shown for shot 1181. The jet has penetrated 8.0 mm of steel. The density contour interval is 0.5 mg/mm$^3$.

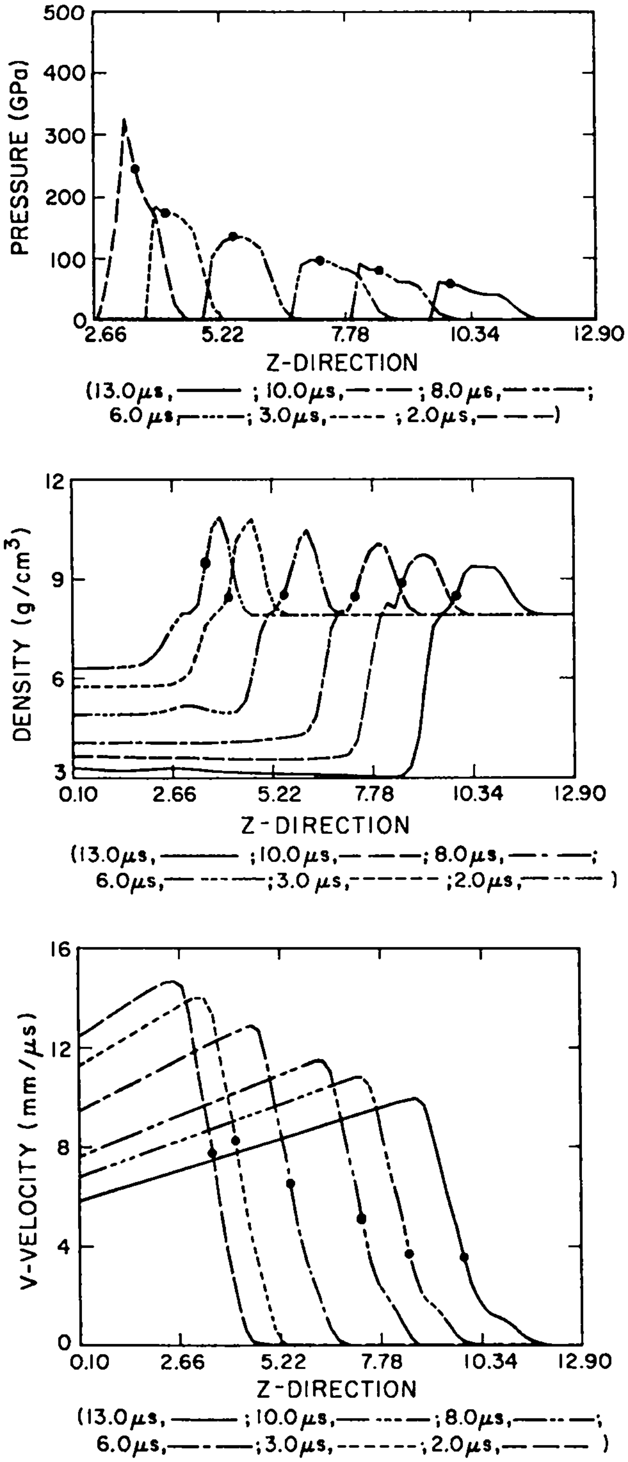

Fig. 5.
Calculated pressures, densities, and vertical velocities near and parallel to the vertical z-axis are shown at various times. The interface cell between the jet and target is located by a star.

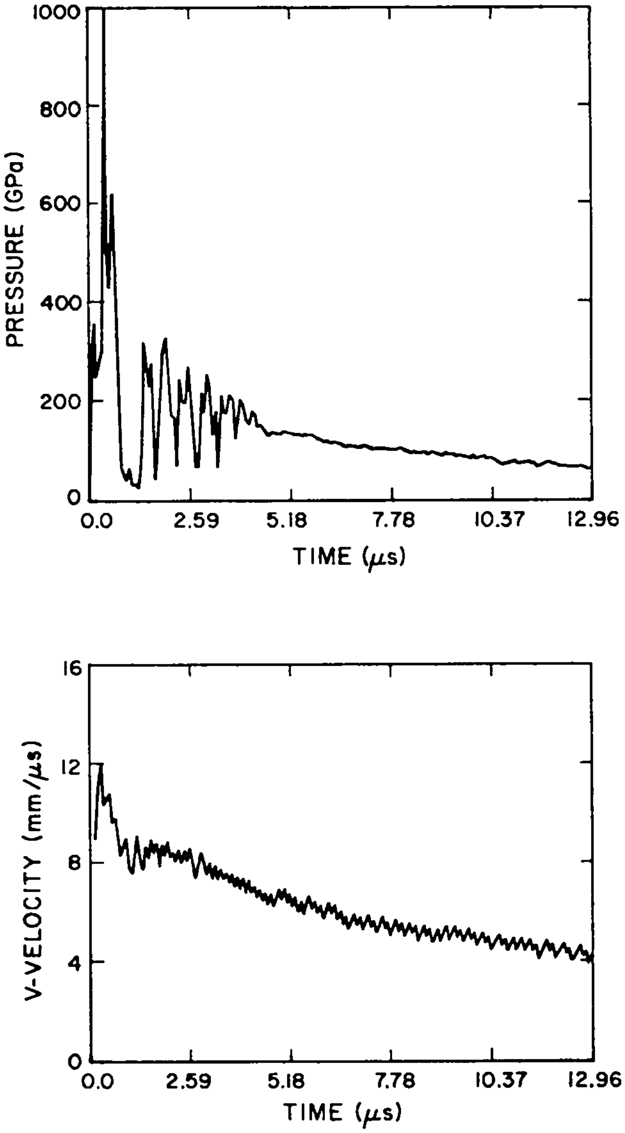

Fig. 6.
Calculated pressure and velocity at the interface between the advancing steel jet tip and the target are shown as a function of time.

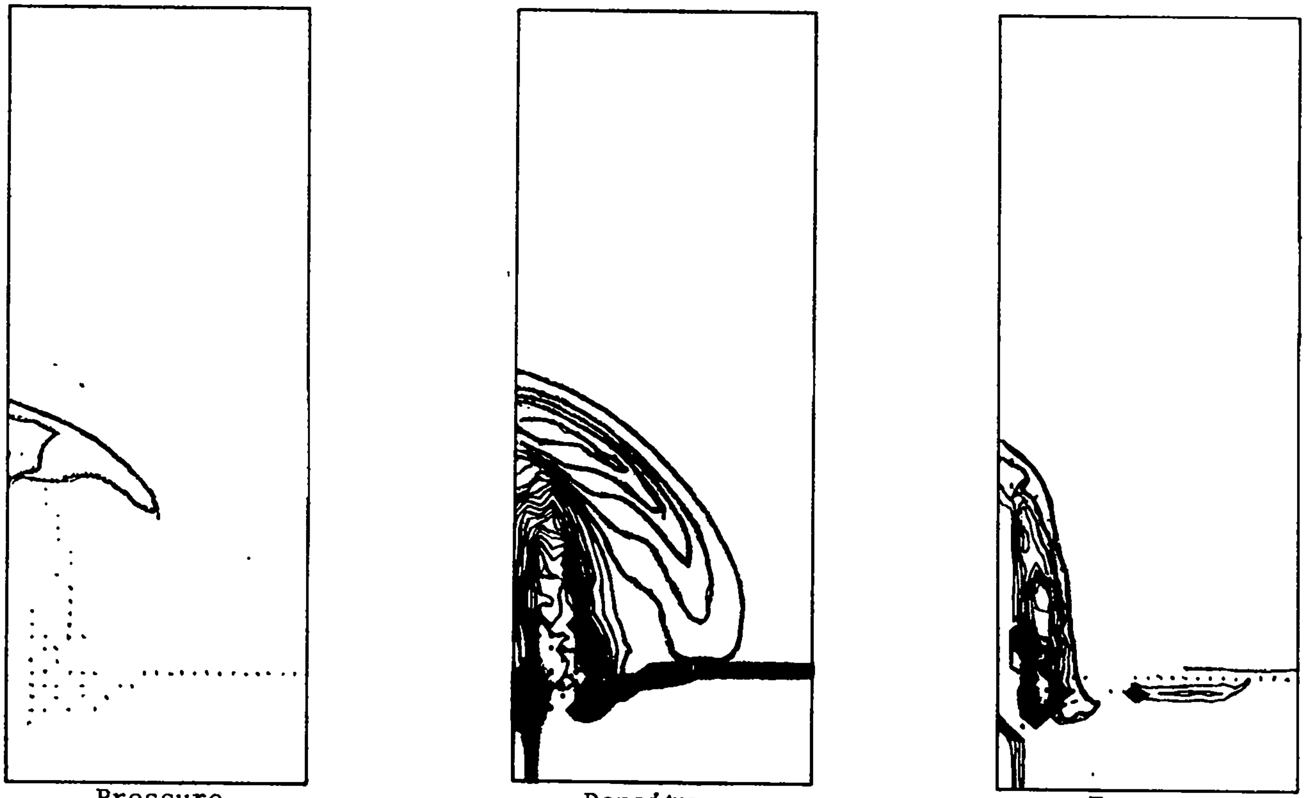

Pressure

Density

Energy

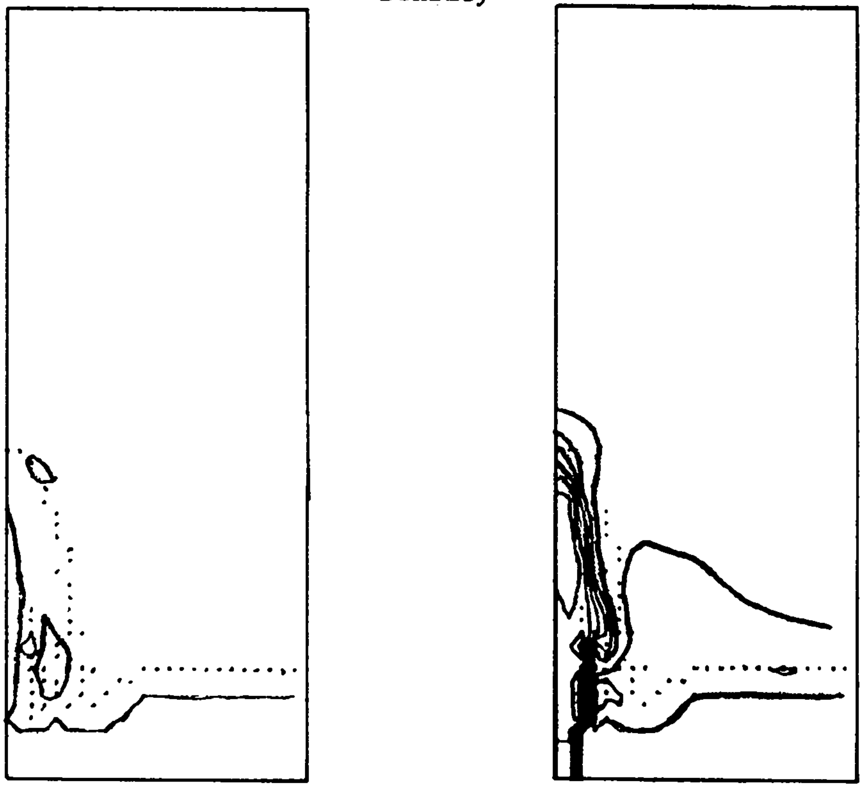

U Velocity

V Velocity

Fig. 7.
Pressure, density, energy, and U and V velocity contours are shown at 6.0 μs for the system shown in Fig. 3. The pressure contour interval is 50 GPa, the energy contour interval is 0.05 Mbar·cm$^3$/g, and the velocity contour interval is 2 mm/μs.

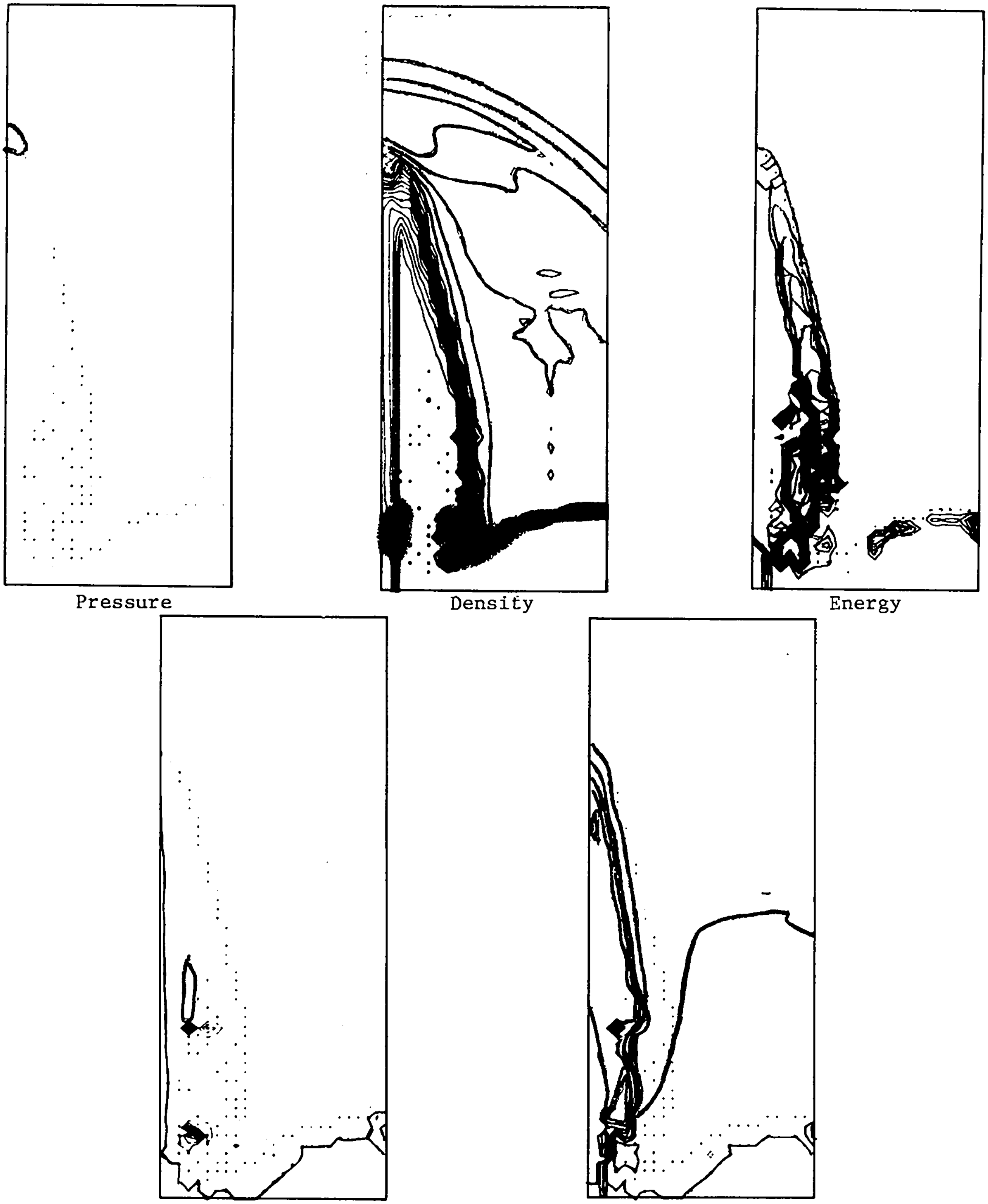

Pressure Density Energy

U Velocity V Velocity

Fig. 8.

Pressure, density, energy, and U and V velocity contours are shown at 13.0 μs for the system illustrated in Fig. 4. The pressure contour interval is 50 GPa, the energy contour interval is 0.05 Mbar·cm$^3$/g, and the velocity interval is 2 mm/μs.

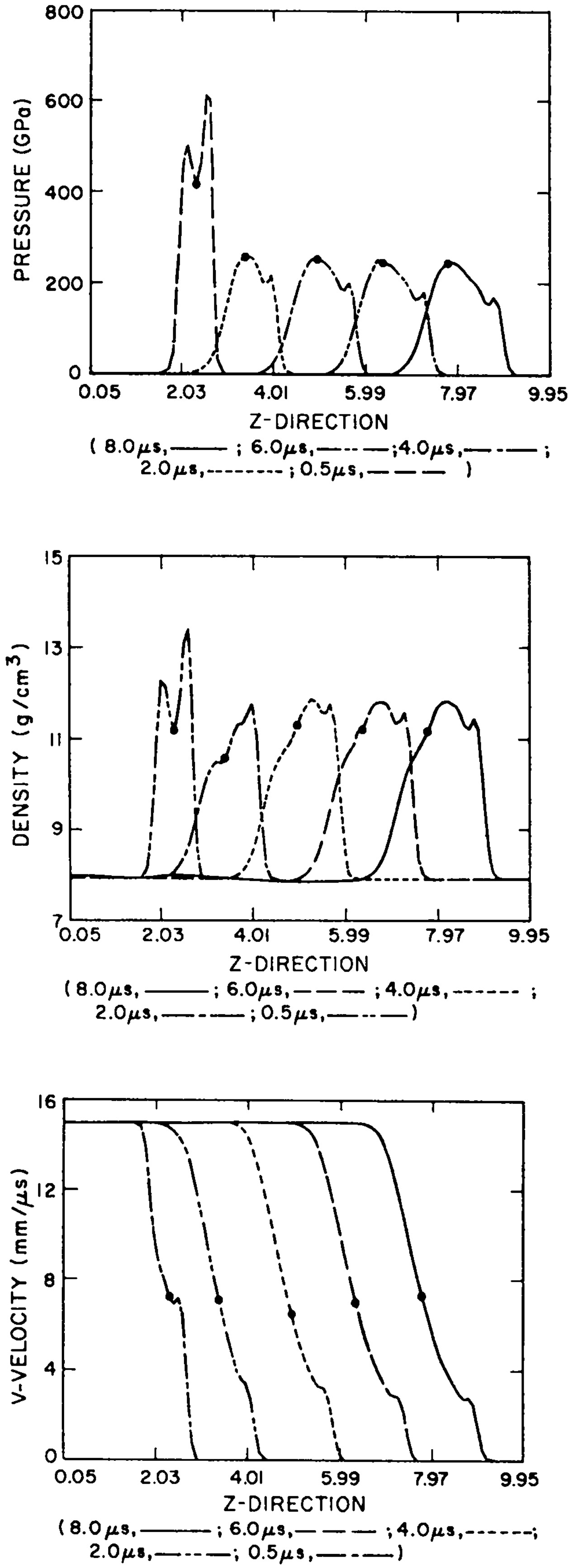

Fig. 9.
Calculated pressures, densities, and vertical velocities along and near the vertical z-axis are shown at various times. The initial velocity of the steel rod was 15 mm/μs. A star indicates the interface cell between the rod and target.

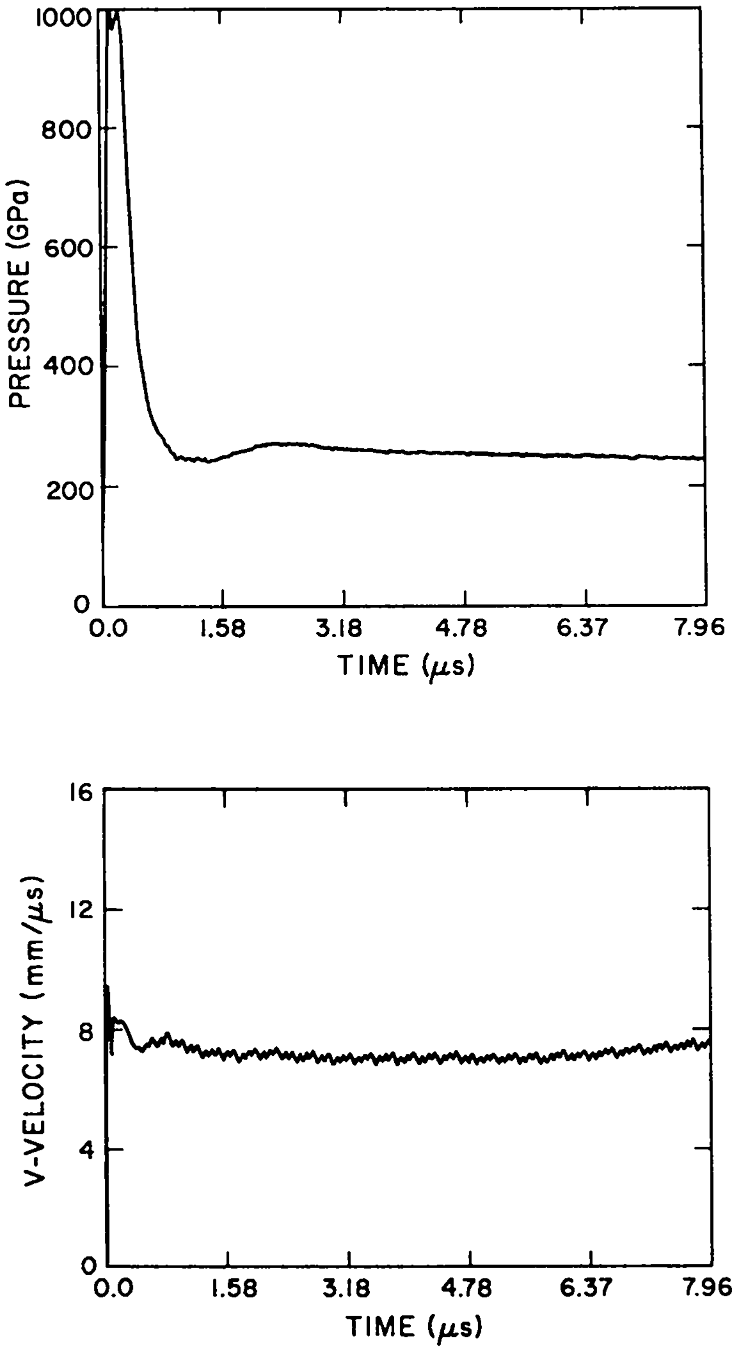

Fig. 10.
Calculated pressure and velocity at the interface between the advancing steel rod tip (whose initial velocity was 15 mm/μs) and the target are shown as functions of time.

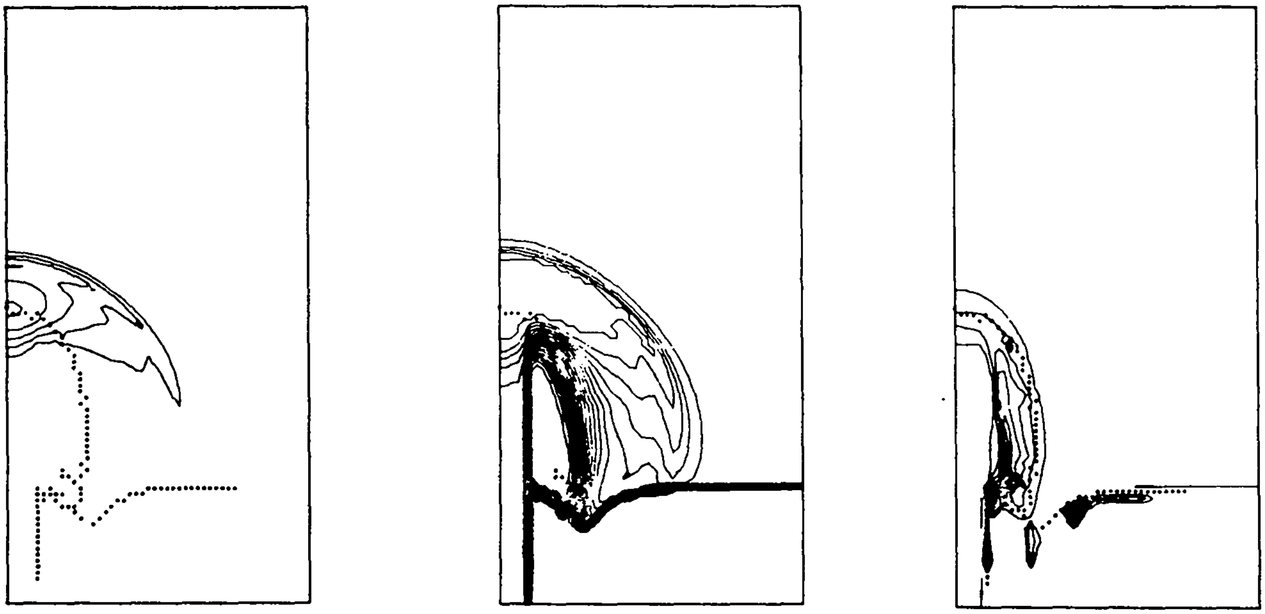

Pressure Density Energy

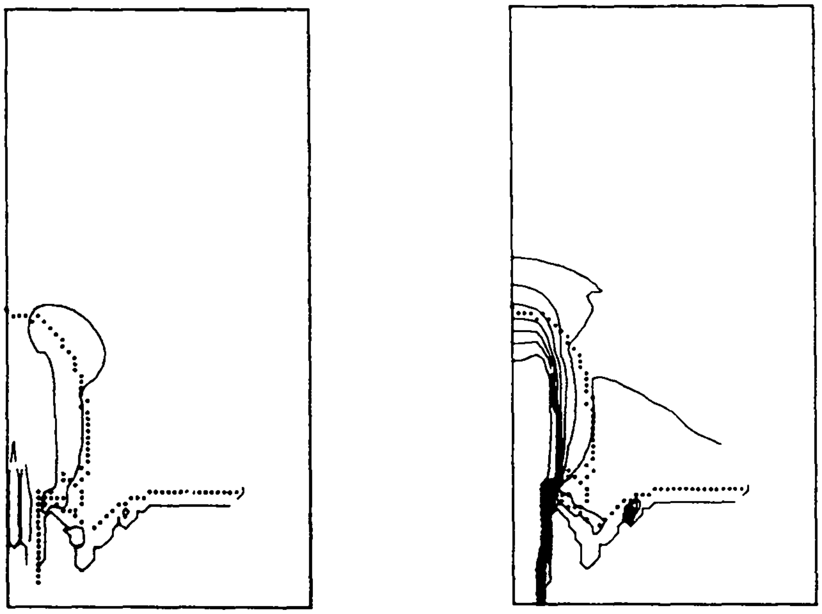

U Velocity V Velocity

Fig. 11.
Pressure, density, energy, and U and V velocity contours at 4.0 μs for a steel rod with a 15-mm/μs initial velocity penetrating a steel target. The pressure contour interval is 50 GPa, the density contour interval is 0.5 mg/mm$^3$, the energy contour interval is 0.05 Mbar · cm$^3$/g, and the velocity contour interval is 2 mm/μs. The graph is 50 mm wide and 110 mm high.

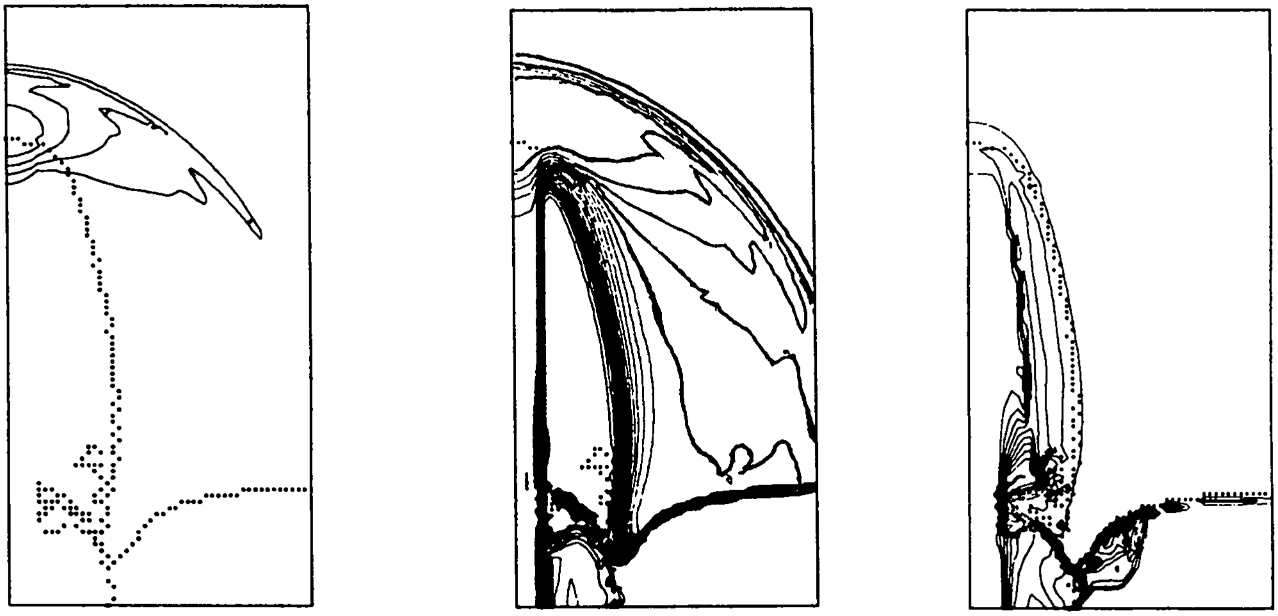

Pressure Density Energy

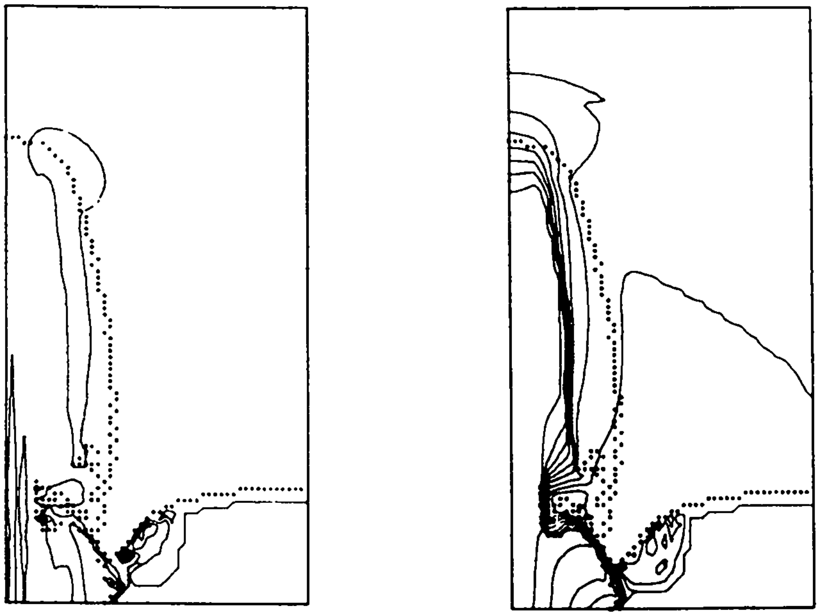

U Velocity V Velocity

Fig. 12.
Pressure, density, energy, and U and V velocity contours at 8.0 μs for a steel rod with a 15-mm/μs initial velocity penetrating a steel target. The pressure contour interval is 50 GPa, the density contour interval is 0.5 mg/mm$^3$, the energy contour interval is 0.05 Mbar · cm$^3$/g, and the velocity contour interval is 2 mm/μs. The graph is 50 mm wide and 100 mm high.

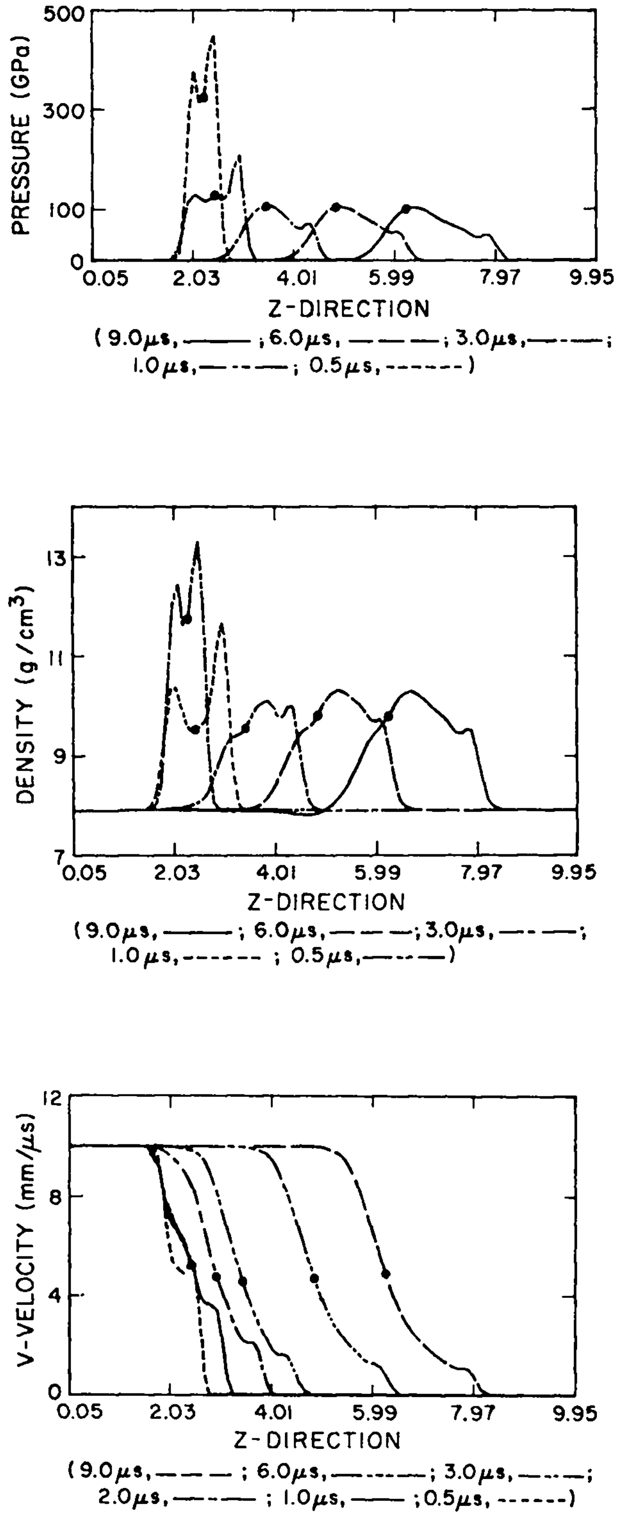

Fig. 13.
Calculated pressure, density, and velocity one-dimensional graphs along the steel rod (with a 10-mm/μs initial velocity) are shown at various times.

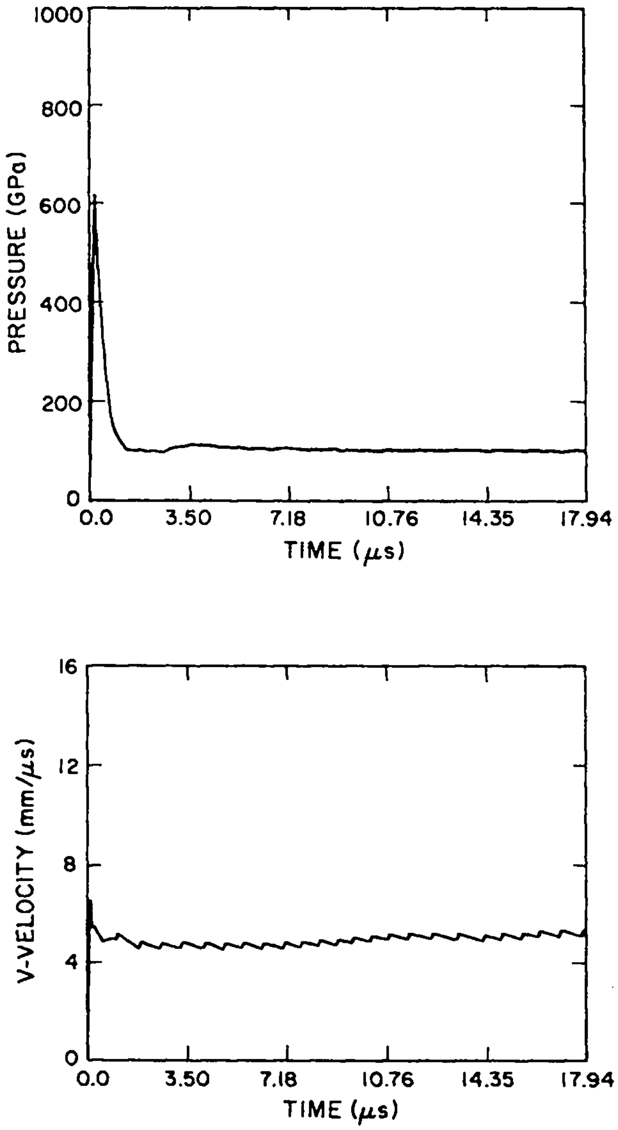

Fig. 14.
Calculated pressure and velocity at the interface between the advancing steel rod tip (with a 10-mm/μs initial velocity) and the target as a function of time.

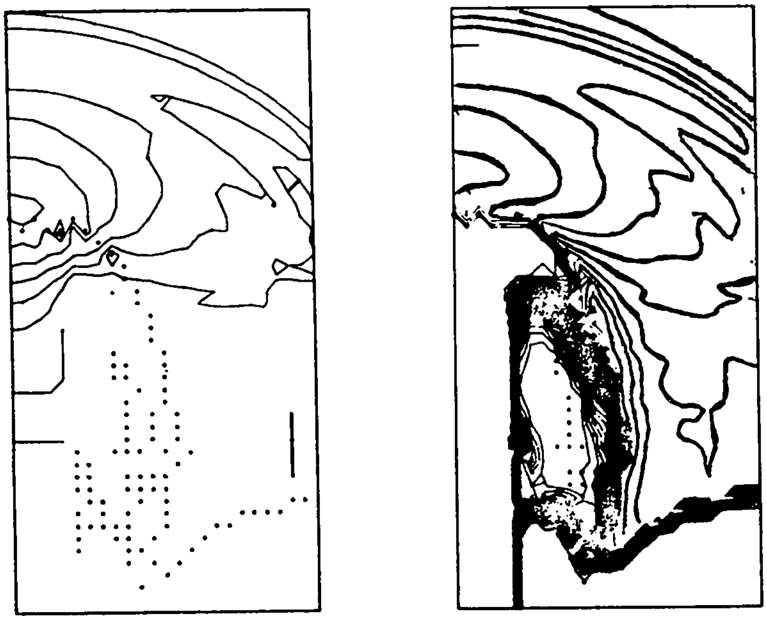

Pressure

Density

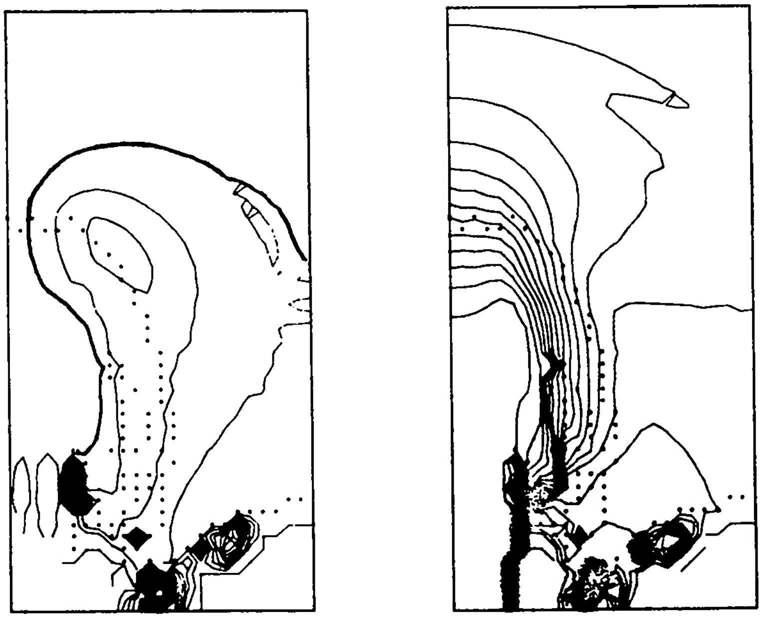

U Velocity

V Velocity

Fig. 15.
Pressure, density, and U and V velocity contours at 6.0 μs for a 5-mm-radius tantalum rod with an initial velocity of 6.4 mm/μs, penetrating a steel target (40 mm high by 25 mm wide). The graph is 25 mm wide and 50 mm high. The pressure contour interval is 10 GPa, the density interval is 0.25 $mg/mm^3$, and the velocity interval is 0.5 mm/μs.

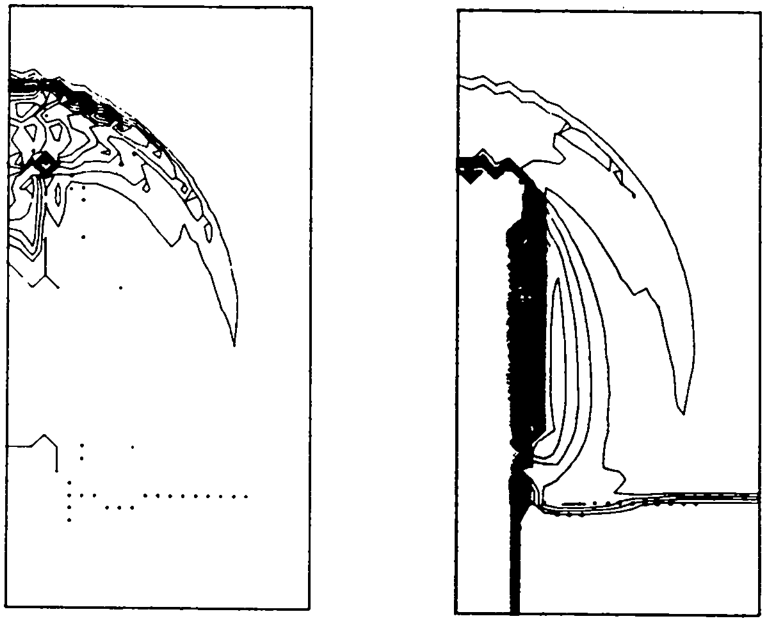

Pressure Density

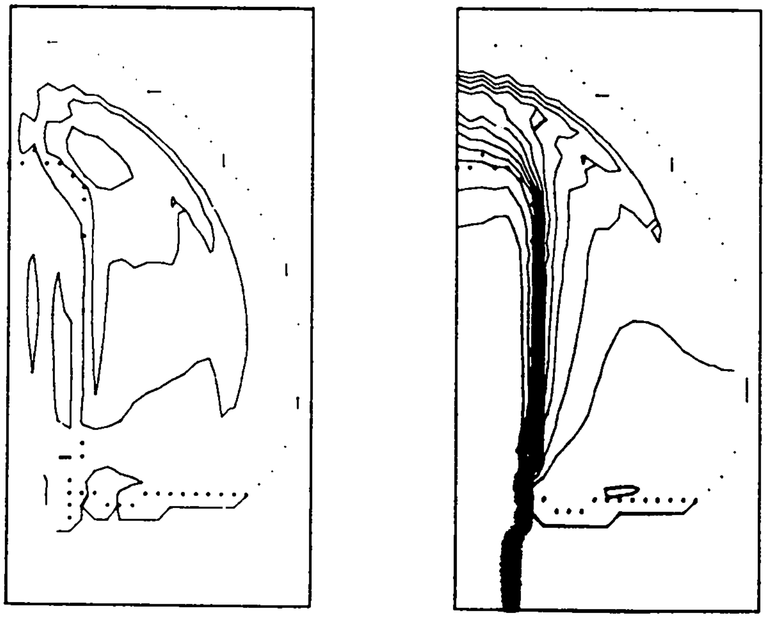

U Velocity V Velocity

Fig. 16.
Pressure, density, and U and V velocity contours at 5.0 μs for a 5-mm-radius tantalum rod, with an initial velocity of 6.4 mm/μs, penetrating a water target (40 mm high by 25 mm wide). The graph is 25 mm wide and 50 mm high. The pressure contour interval is 2 GPa, the density interval is 0.25 mg/mm$^3$, and the velocity interval is 0.5 mm/μs.

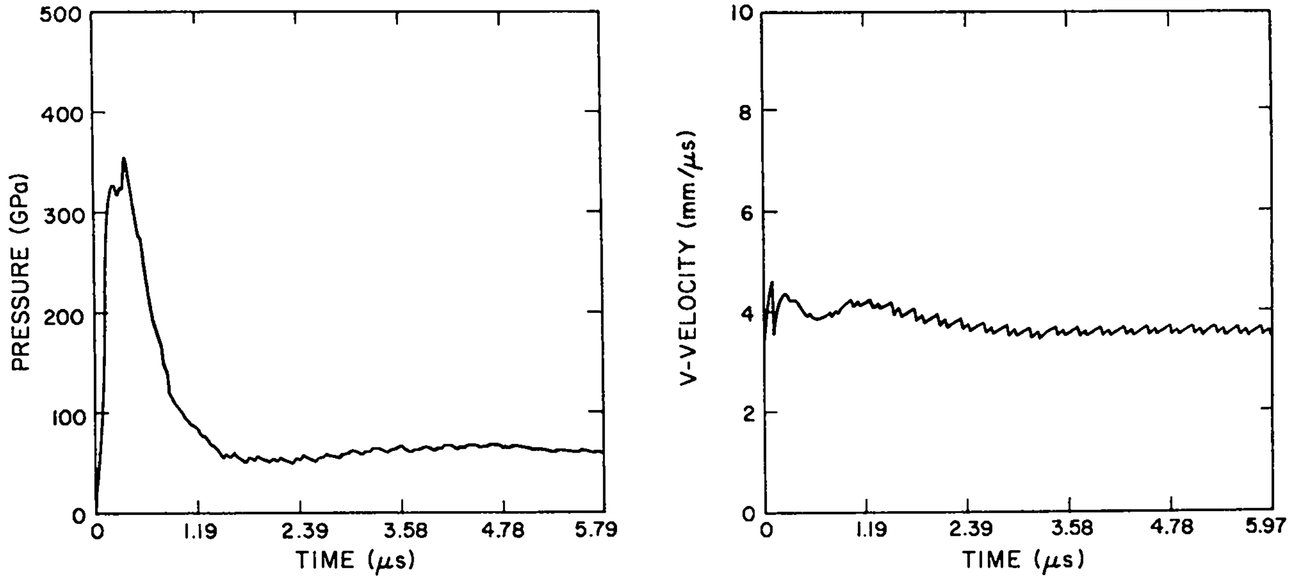

Fig. 17.
Calculated pressure and velocity at the interface between the advancing tantalum rod tip (with an initial velocity of 6.4 mm/μs) and the steel target are shown as functions of time.

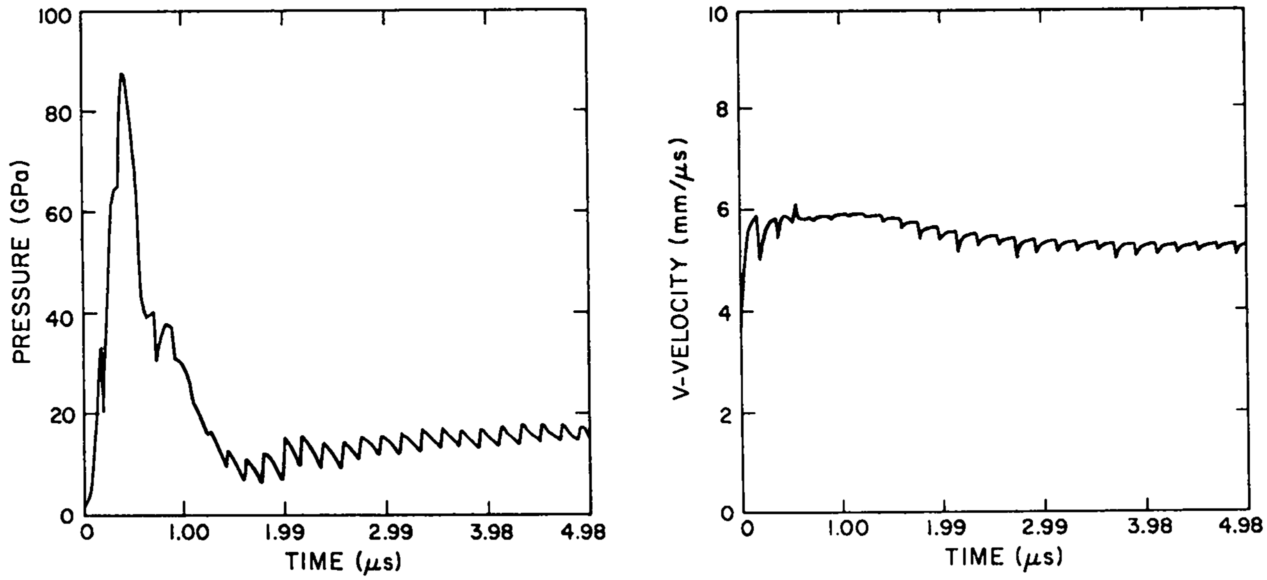

Fig. 18.
Calculated pressure and velocity at the interface between the advancing tantalum rod tip (with an initial velocity of 6.4 mm/μs) and a water target are shown as functions of time.

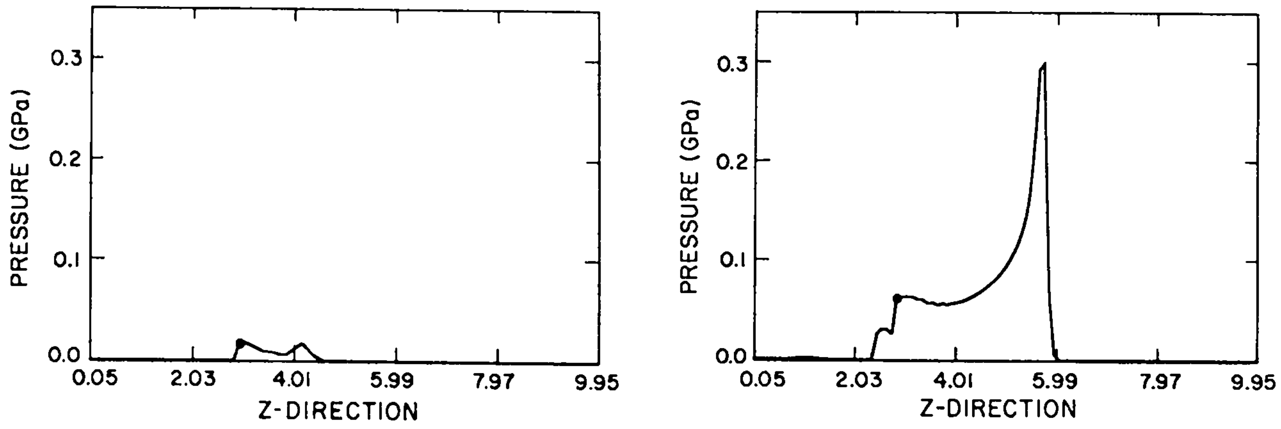

Nonreactive Reactive

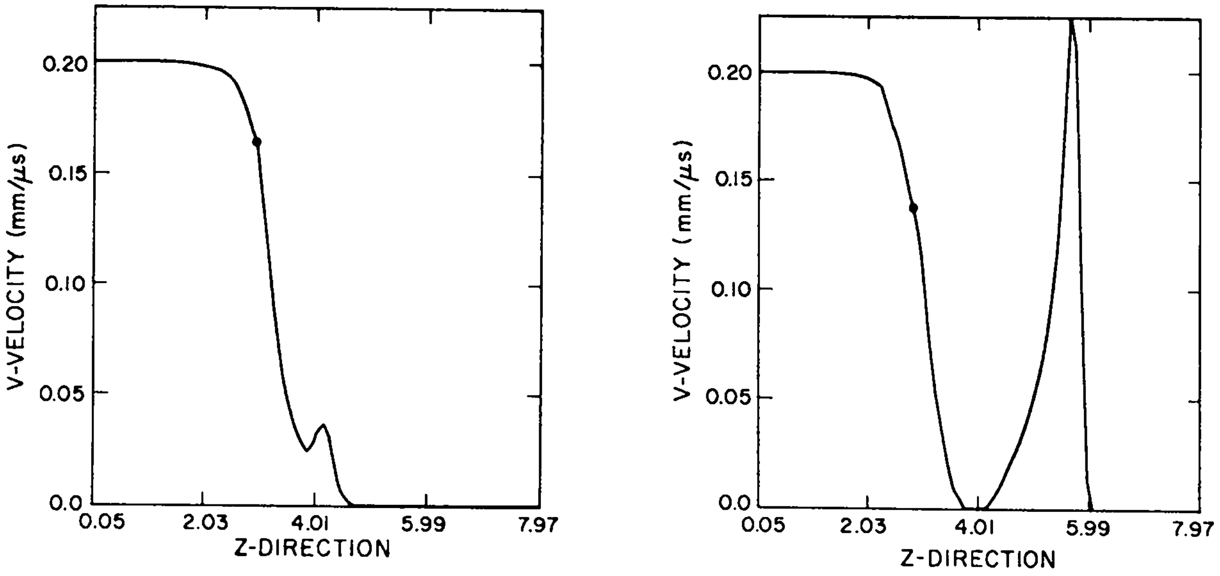

Fig. 19.
Calculated one-dimensional graphs near the axis of the tantalum rod (with a 2.0-mm/μs initial velocity) for a Composition B target, with and without reaction, after 6.0 μs. The interface cell is shown by a star.

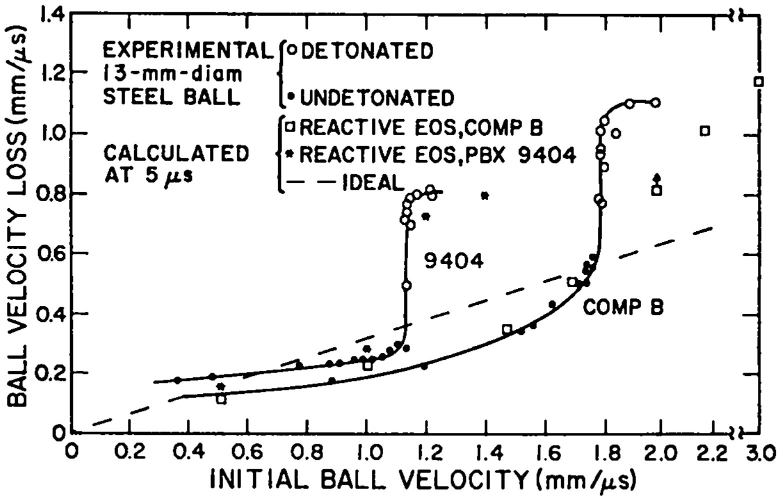

Fig. 20.
Initial ball velocity vs the ball velocity loss for a 13-mm-diam steel ball penetrating PBX 9404 or Composition B-3.

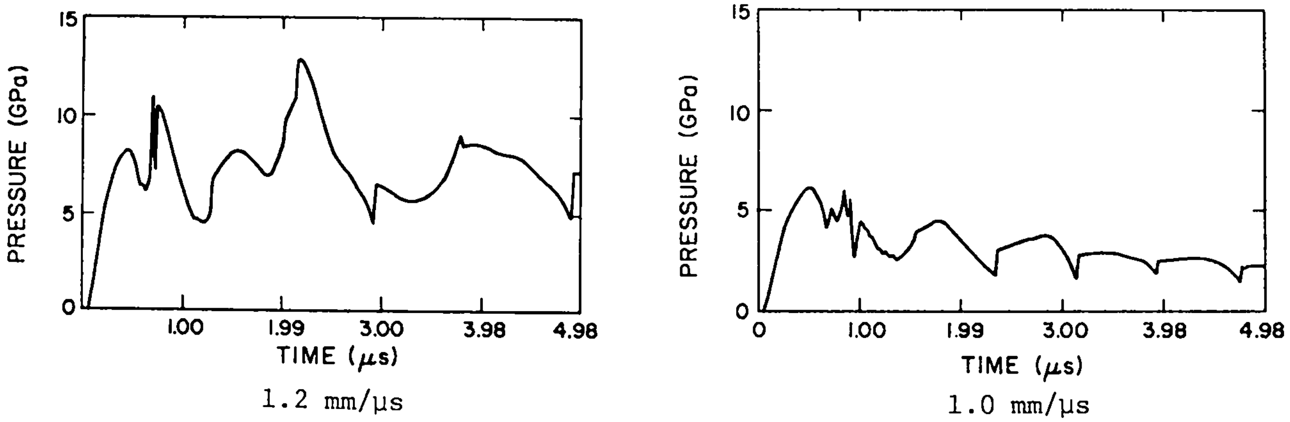

1.2 mm/μs

1.0 mm/μs

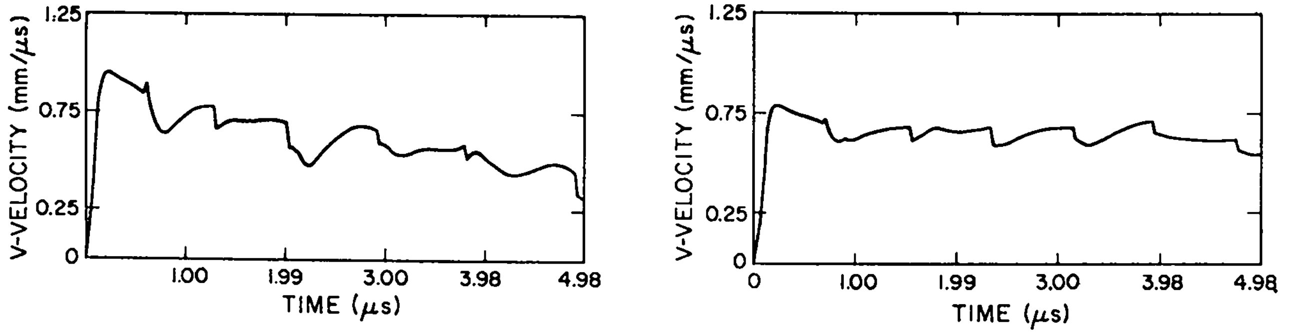

Fig. 21.
Axial interface pressure and velocity as functions of time between a steel ball (initially moving at 1.2 or 1.0 mm/μs) and a PBX-9404 target. The 1.0-mm/μs ball velocity is too slow to cause prompt propagating detonation, whereas the 1.2-mm/μs ball does result in a propagating detonation.

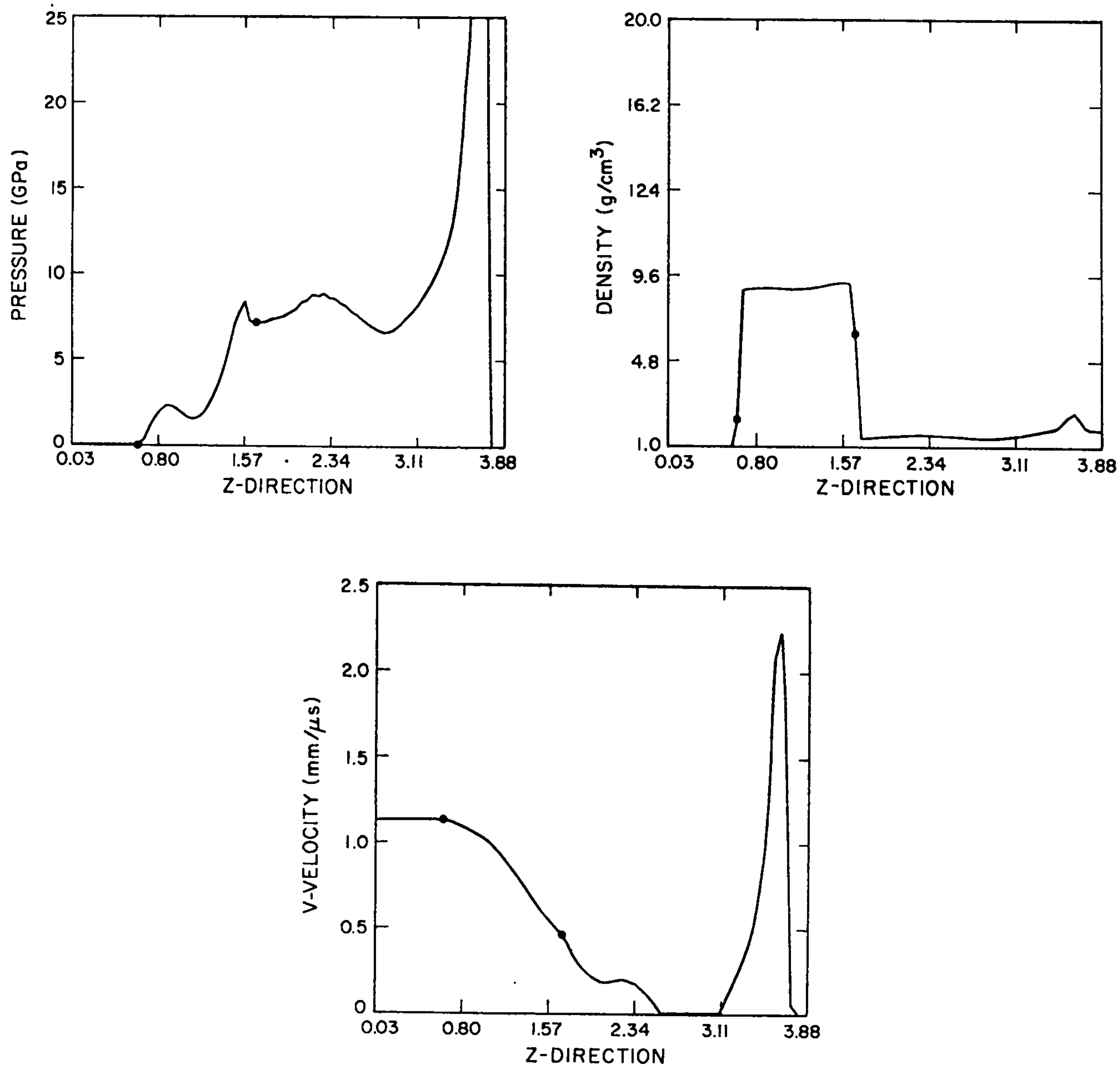

Fig. 22.

Pressure, density, U and V velocity, mass-fraction contours, and the pressure, density, and velocity one-dimensional graphs along and near the vertical z-axis at 4.5 μs for a 1.3-mm steel ball initially moving at 1.2 mm/μs penetrating PBX 9404. The radial dimension is 16.25 mm and the axial dimension is 39.0 mm.

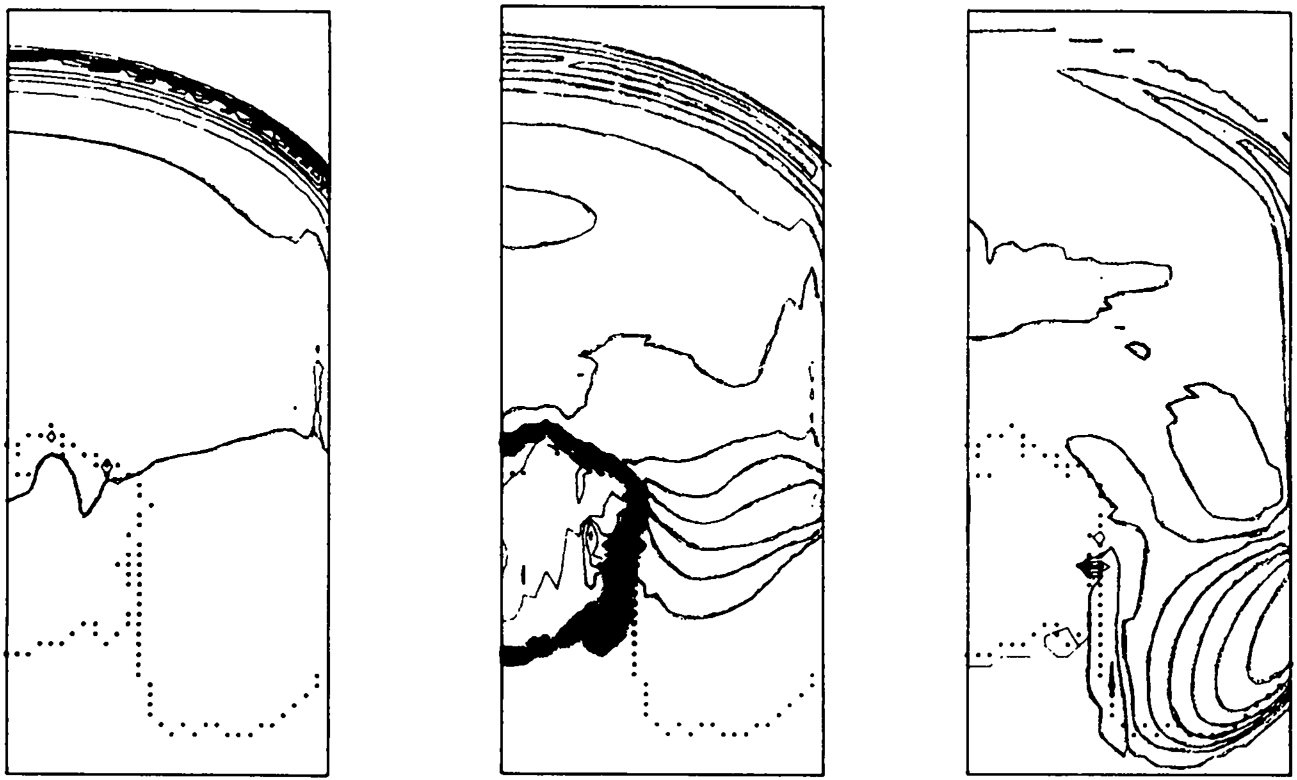

Pressure Density U Velocity

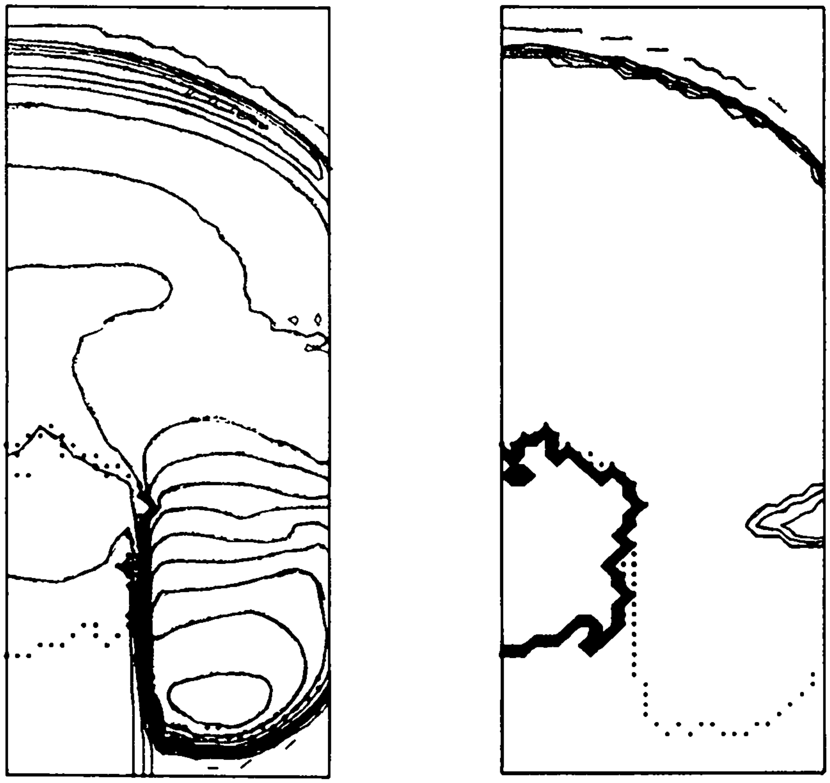

V Velocity Mass Fraction

Fig. 22 (cont).

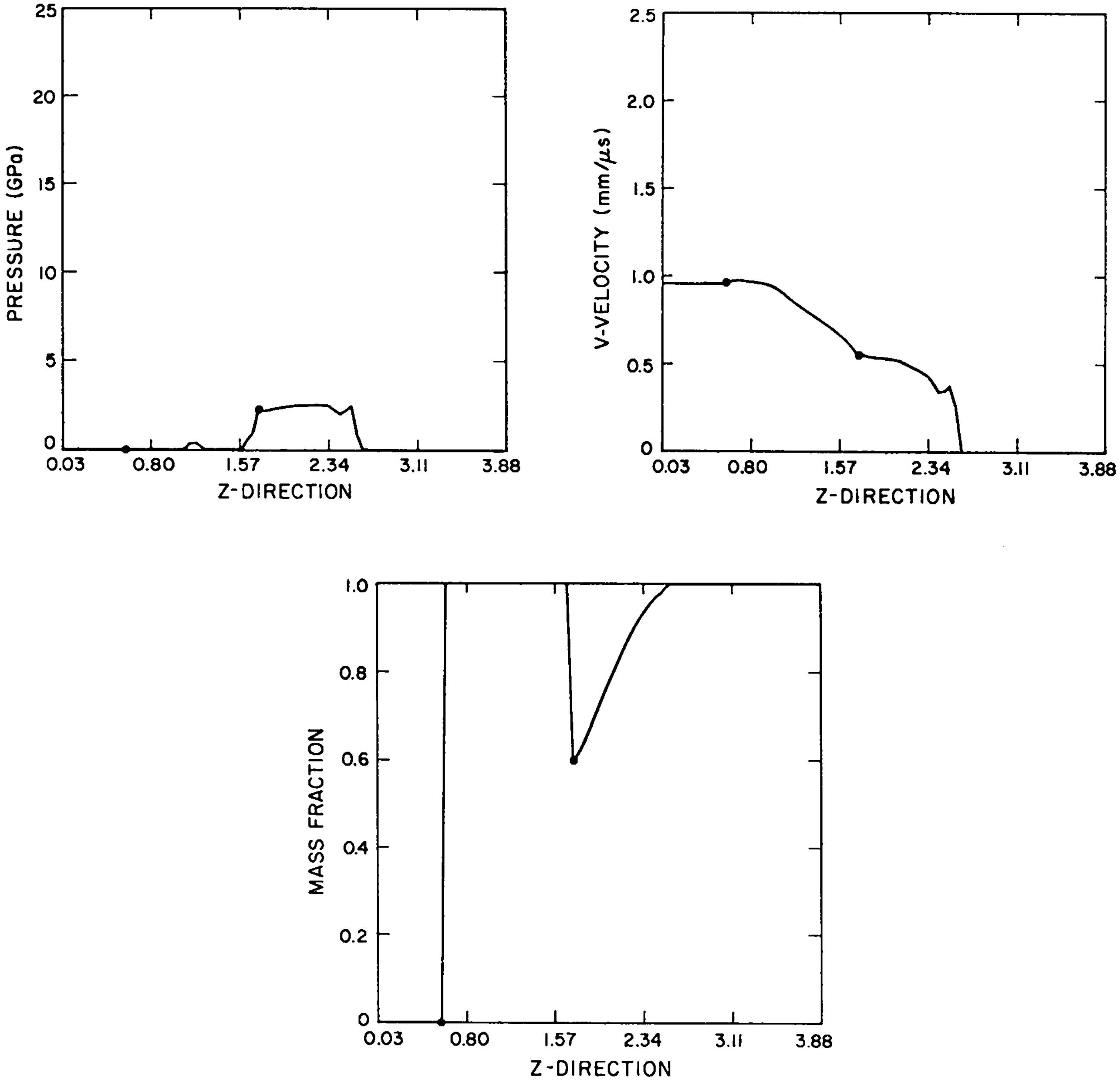

Fig. 23.

Pressure, density, and mass fraction contours and the pressure, velocity, and mass-fraction one-dimensional graphs, along and near the vertical z-axis, at 5.0 μs, for a 1.3-mm steel ball initially moving at 1.0 mm/μs penetrating PBX 9404. The radial dimension is 16.25 mm and the axial dimension is 39.0 mm.

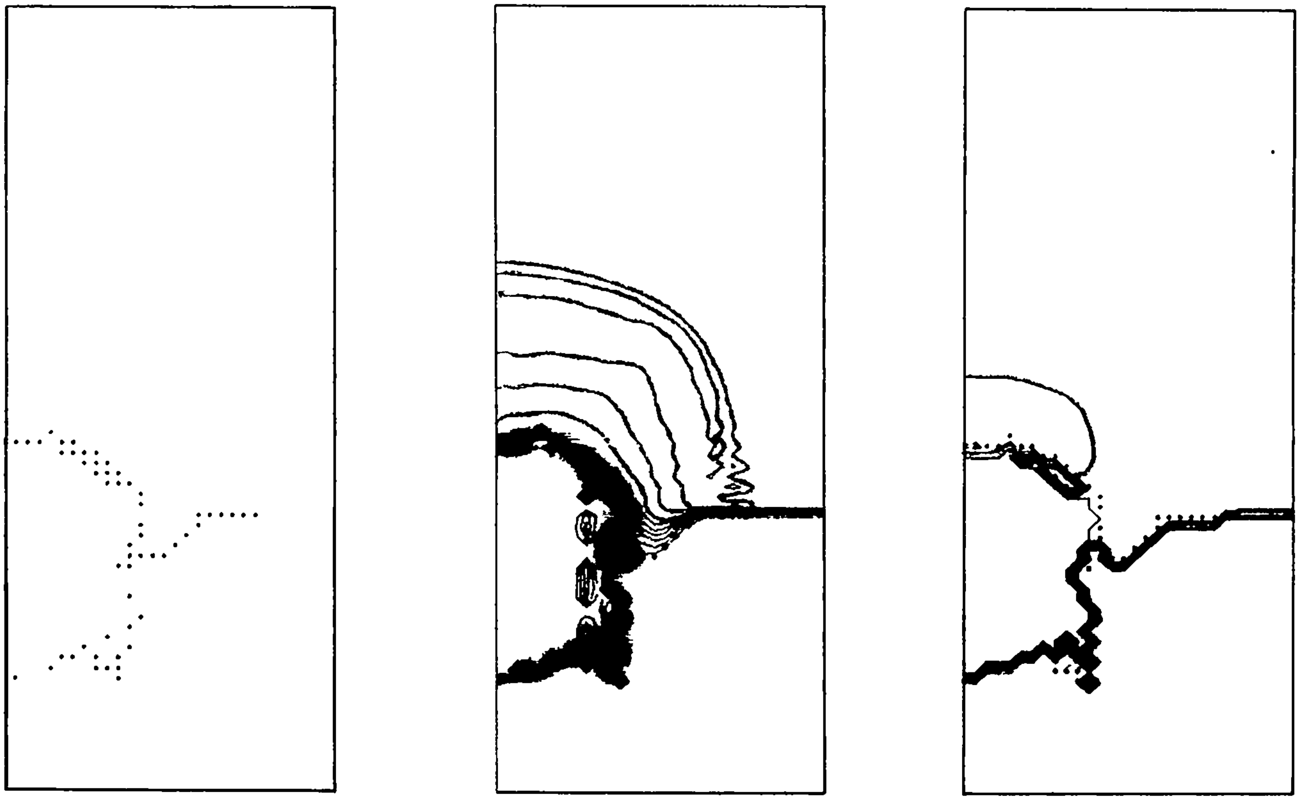

Pressure

Density

Mass Fraction

Fig. 23.(cont)

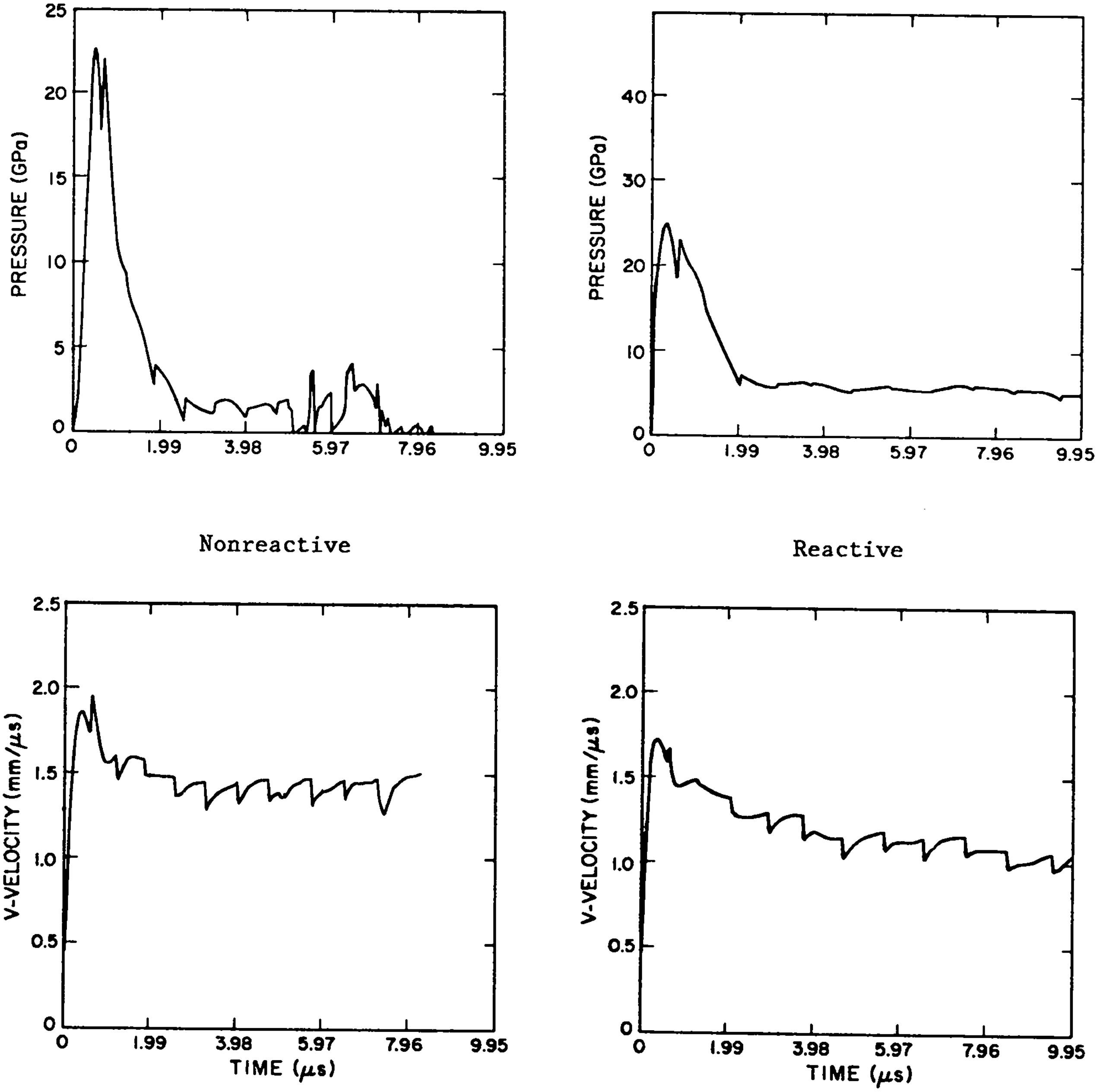

Fig. 24.
Interface pressure and velocity at the tip of a 6.5-mm-radius steel rod initially moving at 2.0 mm/μs into reactive and nonreactive Composition B.

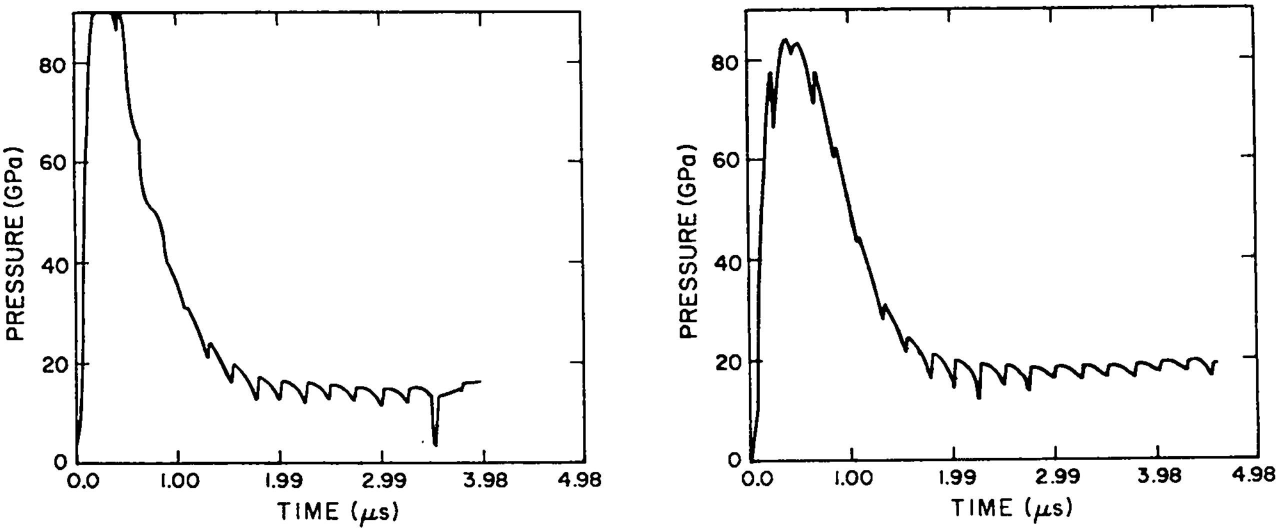

Nonreactive

Reactive

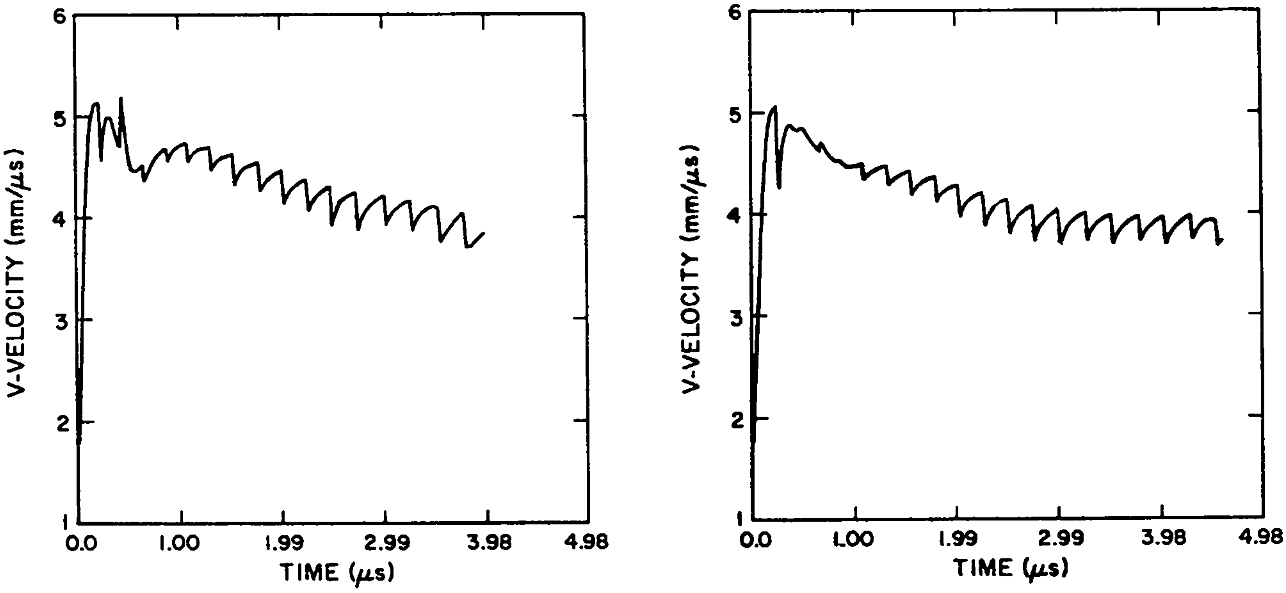

Fig. 25.
Interface pressure and velocity at the tip of a 6.5-mm-radius steel rod initially moving at 6.0 mm/μs penetrating reactive and nonreactive Composition B.

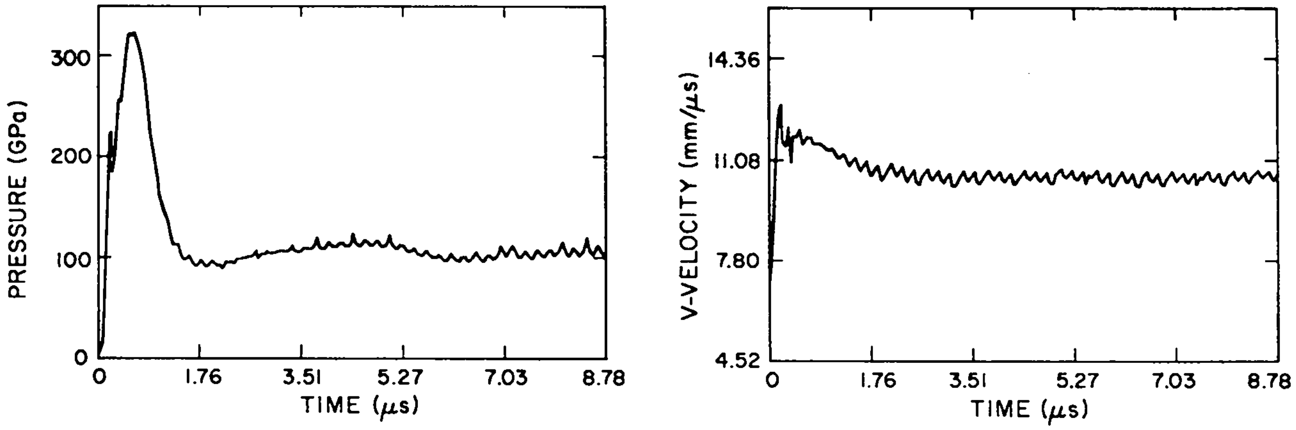

Fig. 26.
Interface pressure and velocity at the tip of a 16-mm-diam steel rod initially moving at 15 mm/μs penetrating PBX 9404.

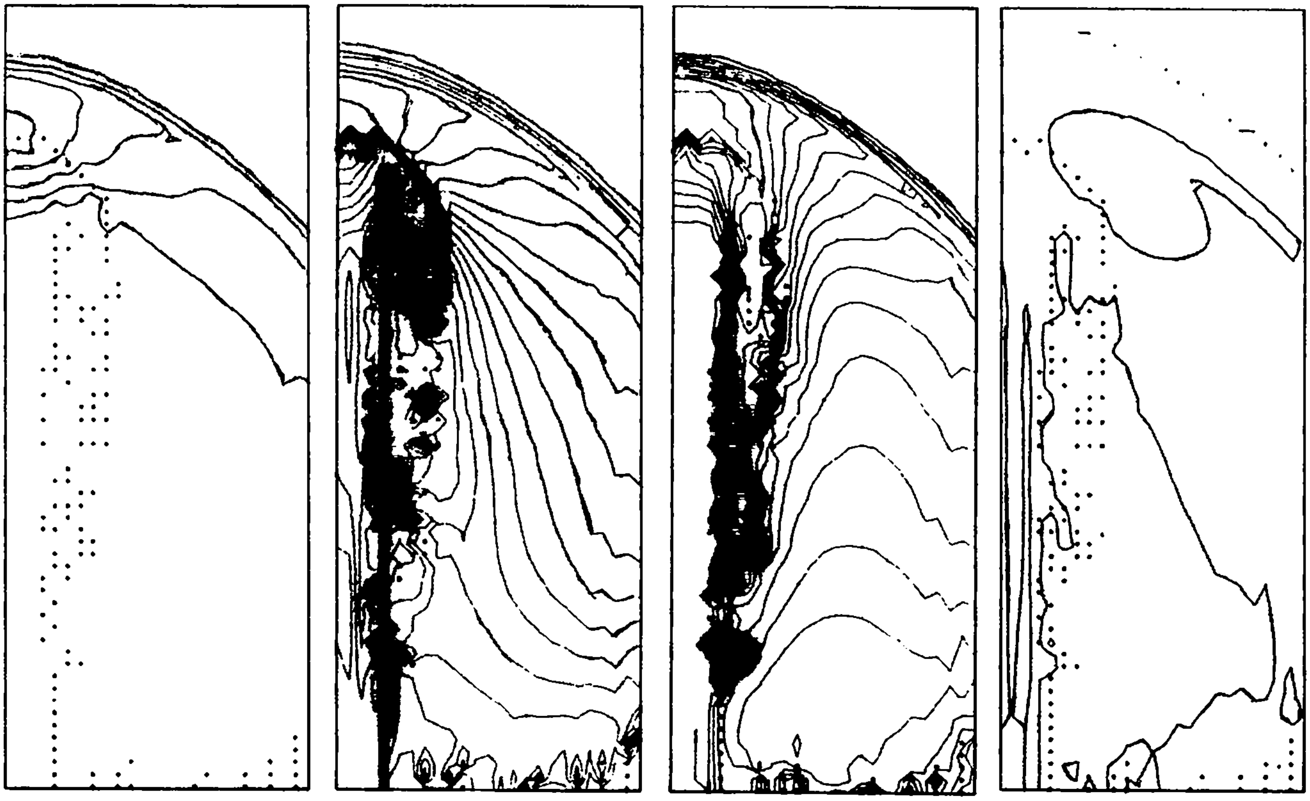

Pressure Density Energy U Velocity

Fig. 27.
Pressure, density, energy, U and V velocity and mass-fraction contours, and the pressure, density, and velocity one-dimensional graphs, along and near the vertical z-axis, at 8.8 μs, for a 16-mm-diam steel rod initially moving at 15 mm/μs penetrating PBX 9404.

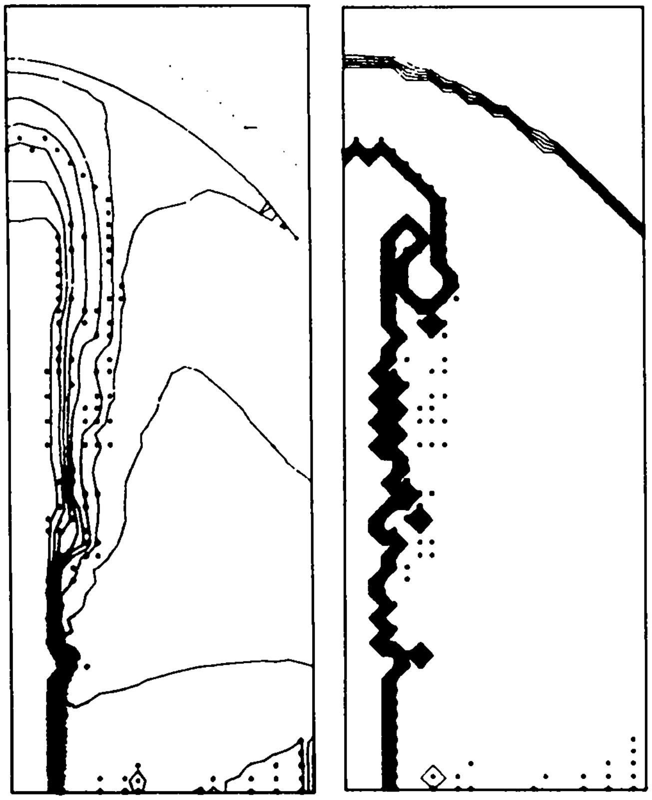

V Velocity

Mass Fraction

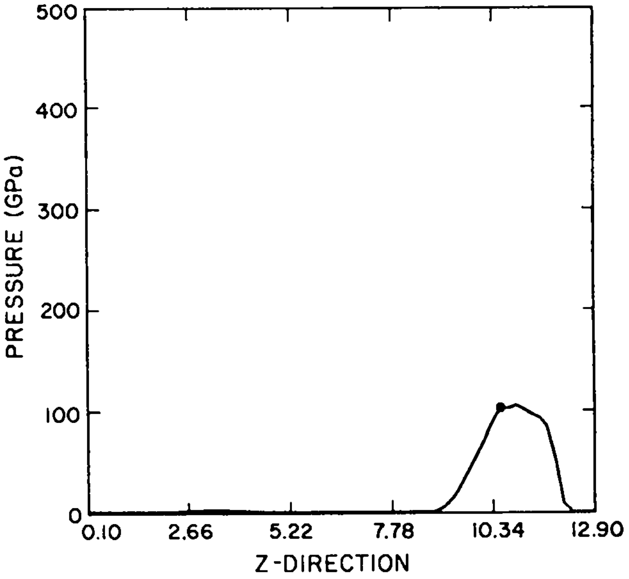

Fig. 27. (cont)

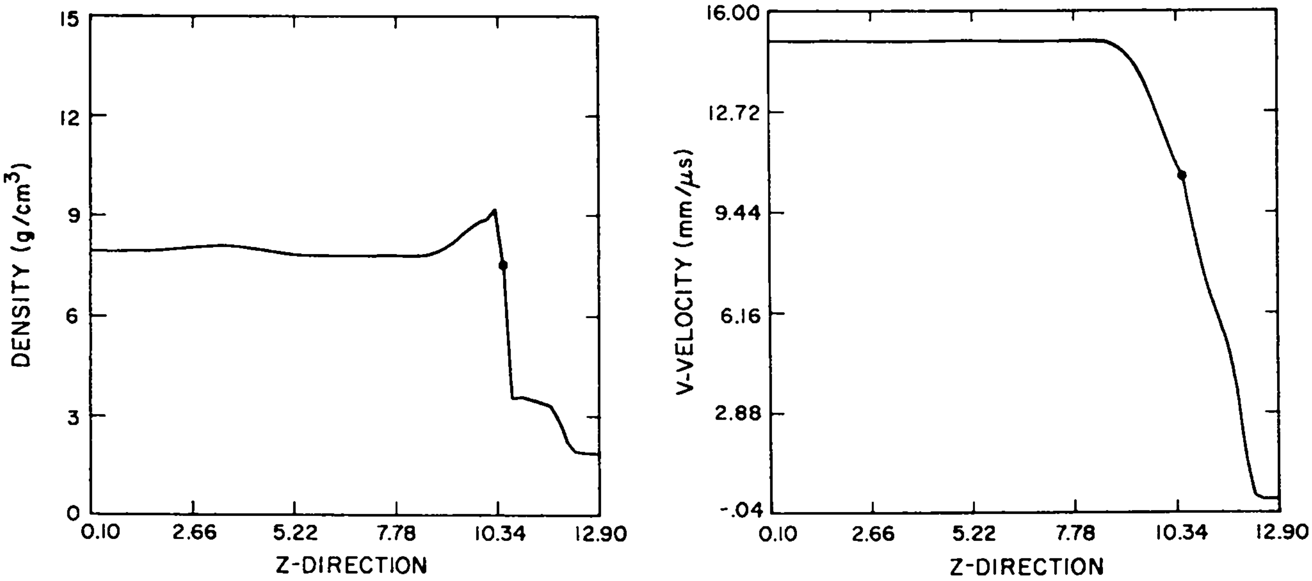

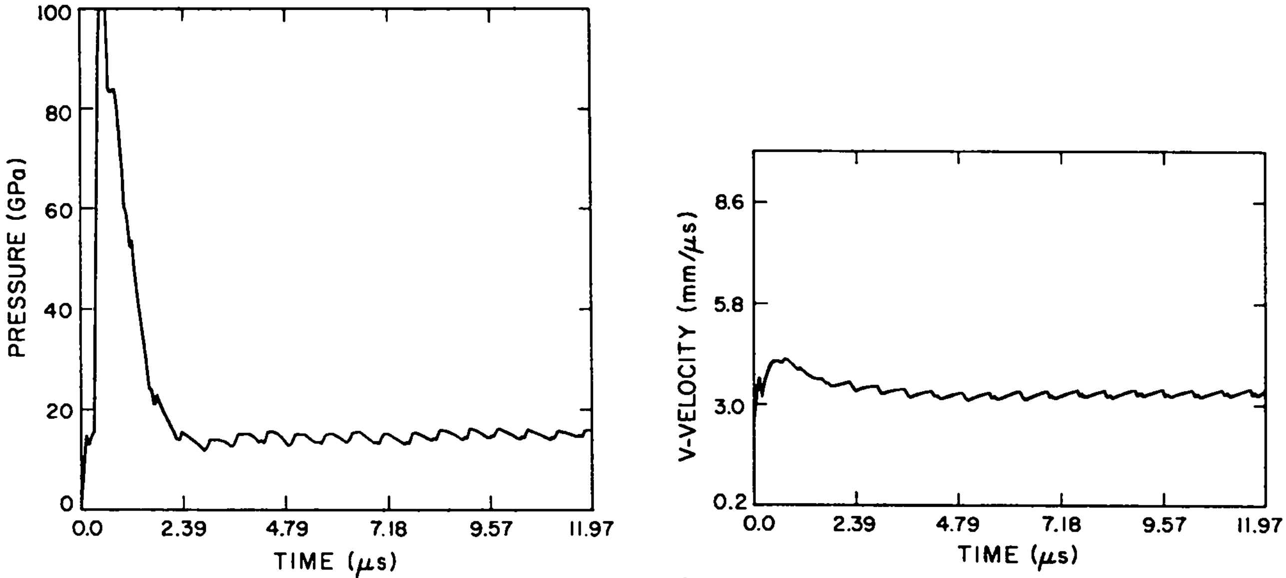

Fig. 28.
Interface pressure and velocity at the tip of an 16-mm-diam steel rod initially moving at 5 mm/μs penetrating PBX 9404.

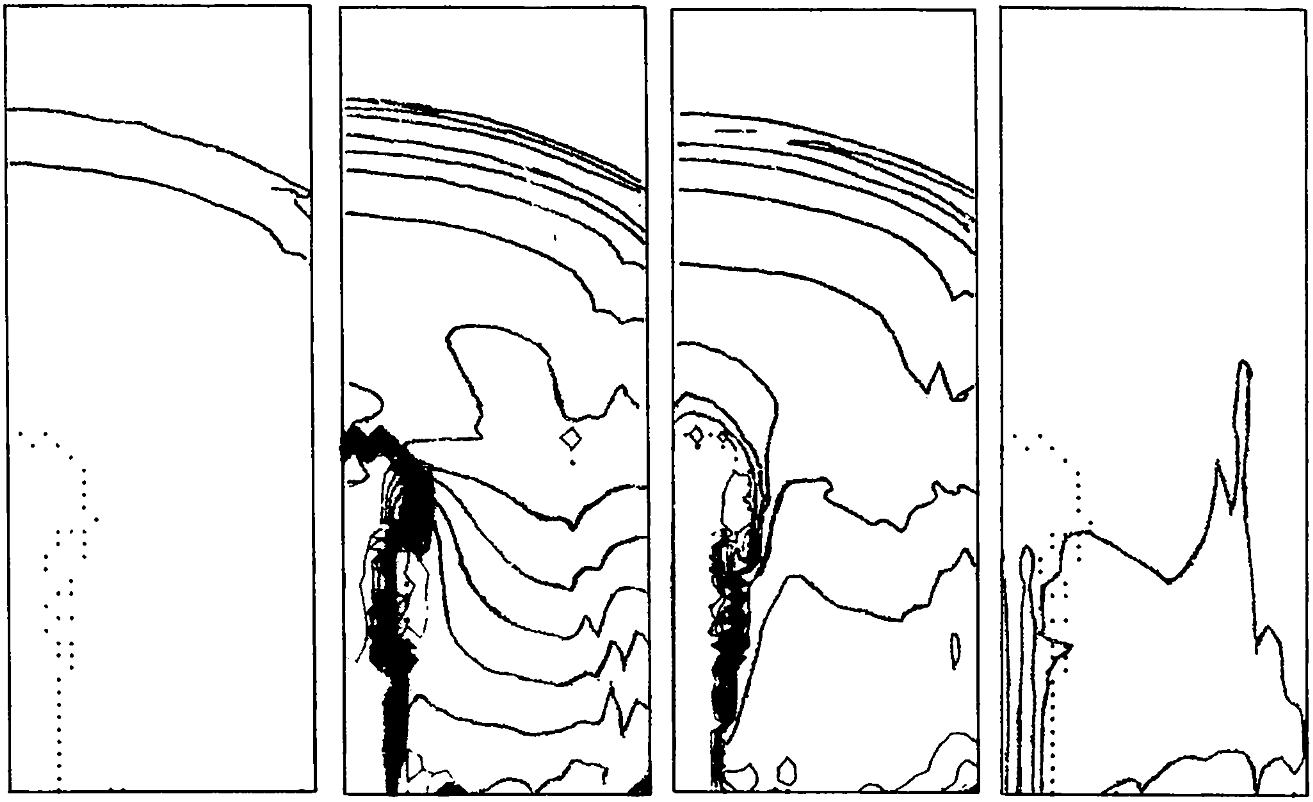

Pressure Density Energy U Velocity

Fig. 29.
Pressure, density, energy, U and V velocity and mass-fraction contours, and the pressure, density, and velocity one-dimensional graphs, along and near the vertical z-axis, at 12.0 μs, for a 16-mm-diam steel rod initially moving at 5 mm/μs penetrating PBX 9404.

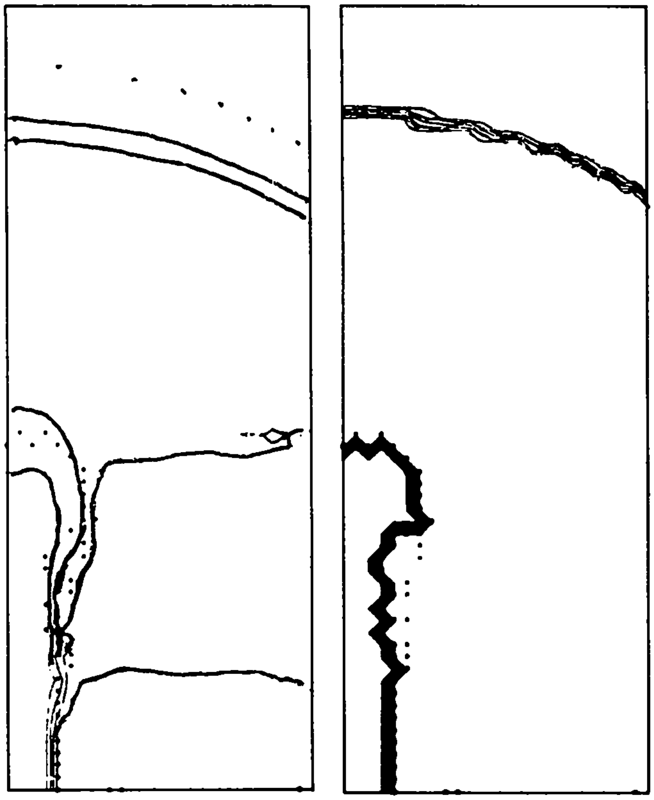

V Velocity

Mass Fraction

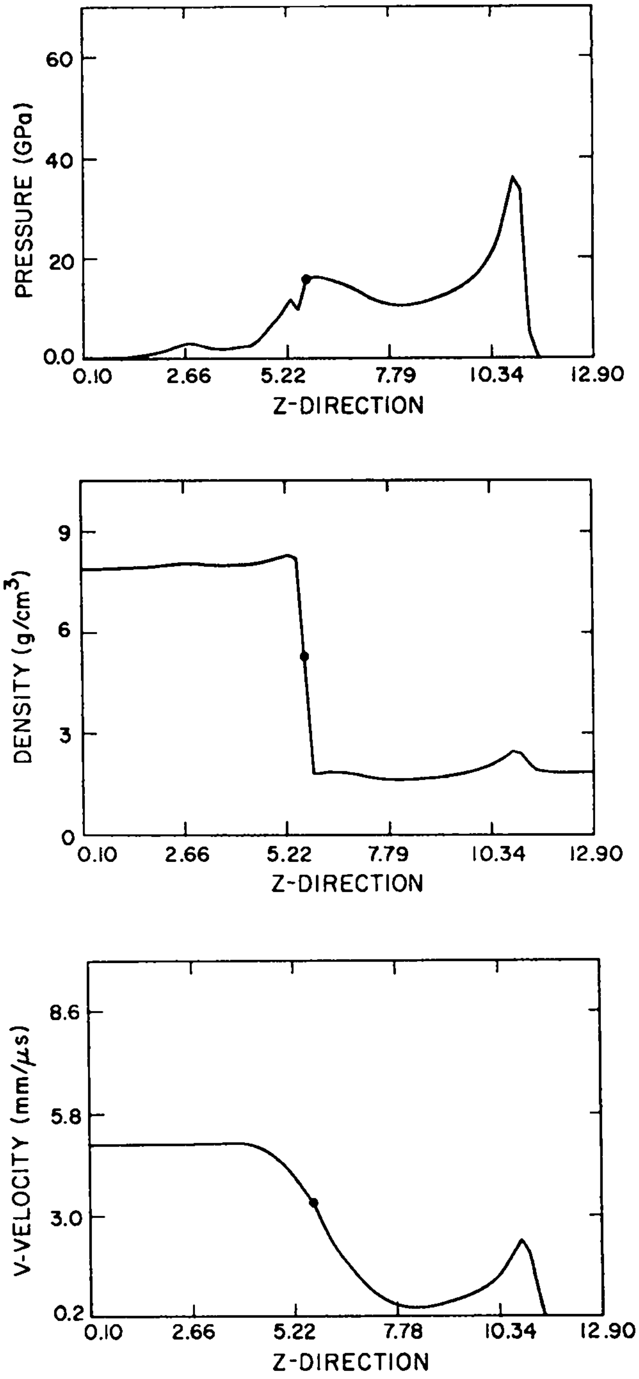

Fig. 29. (cont)

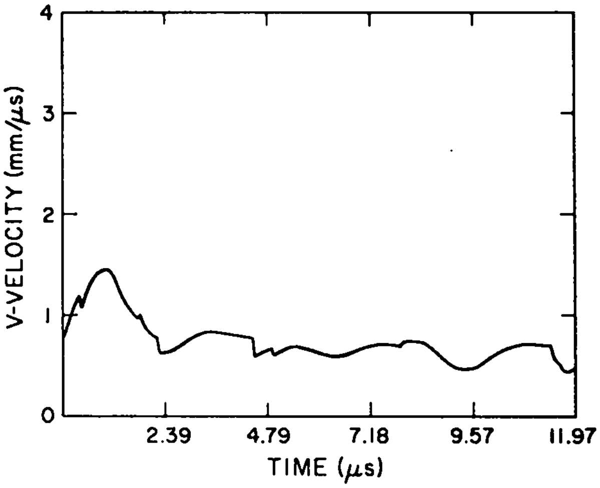

Fig. 30.
Interface velocity at the rod tip for a 16-mm-diam steel rod initially moving at 1.5 mm/μs penetrating PBX 9404.

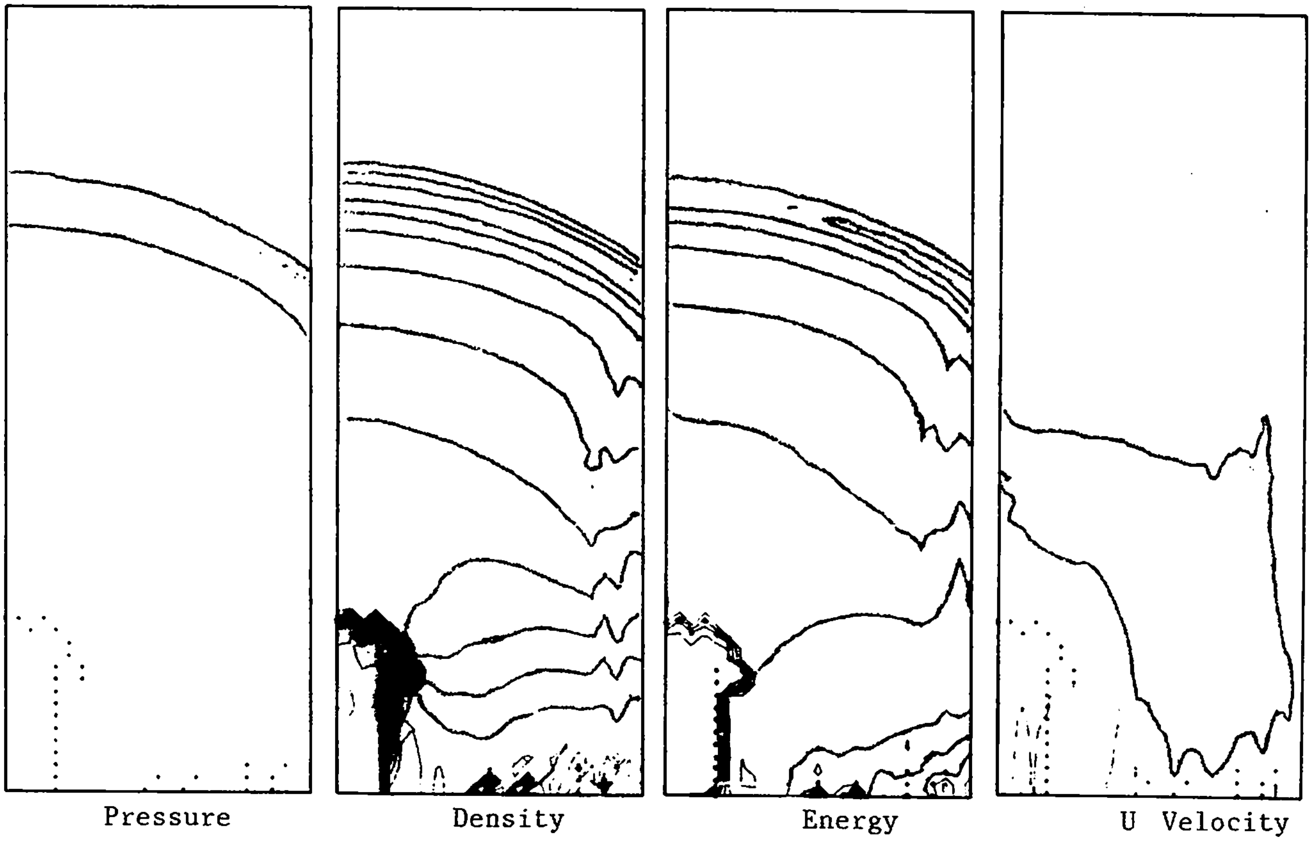

Fig. 31.
Pressure, density, energy, U and V velocity, and mass-fraction contours and the pressure, density, and velocity one-dimensional graphs along and near the vertical z-axis, at 12.0 μs for a 16-mm-diam steel rod initially moving at 1.5 mm/μs penetrating PBX 9404.

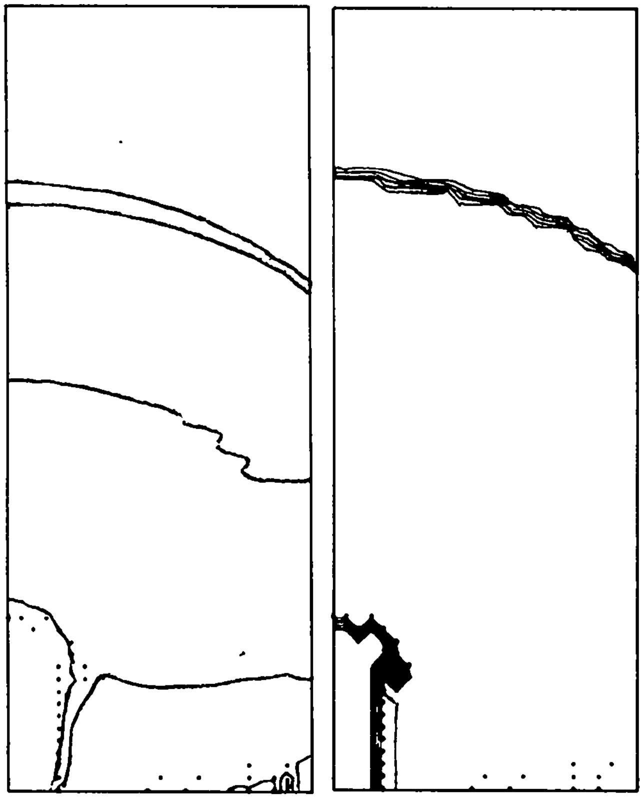

V Velocity    Mass Fraction

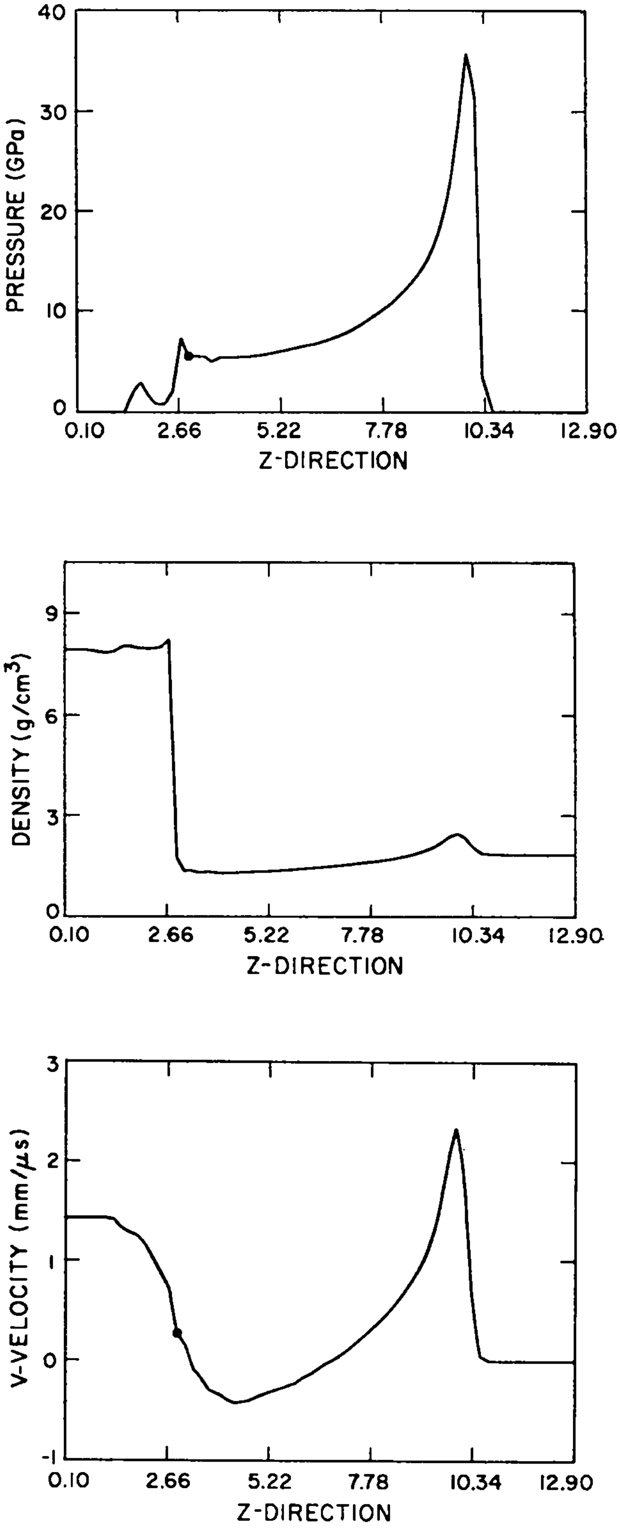

Fig. 31. (cont)

Printed in the United States of America
Available from
National Technical Information Service
US Department of Commerce
5285 Port Royal Road
Springfield, VA 22161

Microfiche (A01)

| Page Range | NTIS Price Code | Page Range | NTIS Price Code | Page Range | NTIS Price Code | Page Range | NTIS Price Code |
|---|---|---|---|---|---|---|---|
| 001-025 | A02 | 151-175 | A08 | 301-325 | A14 | 451-475 | A20 |
| 026-050 | A03 | 176-200 | A09 | 326-350 | A15 | 476-500 | A21 |
| 051-075 | A04 | 201-225 | A10 | 351-375 | A16 | 501-525 | A22 |
| 076-100 | A05 | 226-250 | A11 | 376-400 | A17 | 526-550 | A23 |
| 101-125 | A06 | 251-275 | A12 | 401-425 | A18 | 551-575 | A24 |
| 126-150 | A07 | 276-300 | A13 | 426-450 | A19 | 576-600 | A25 |
| | | | | | | 601-up* | A99 |

*Contact NTIS for a price quote.

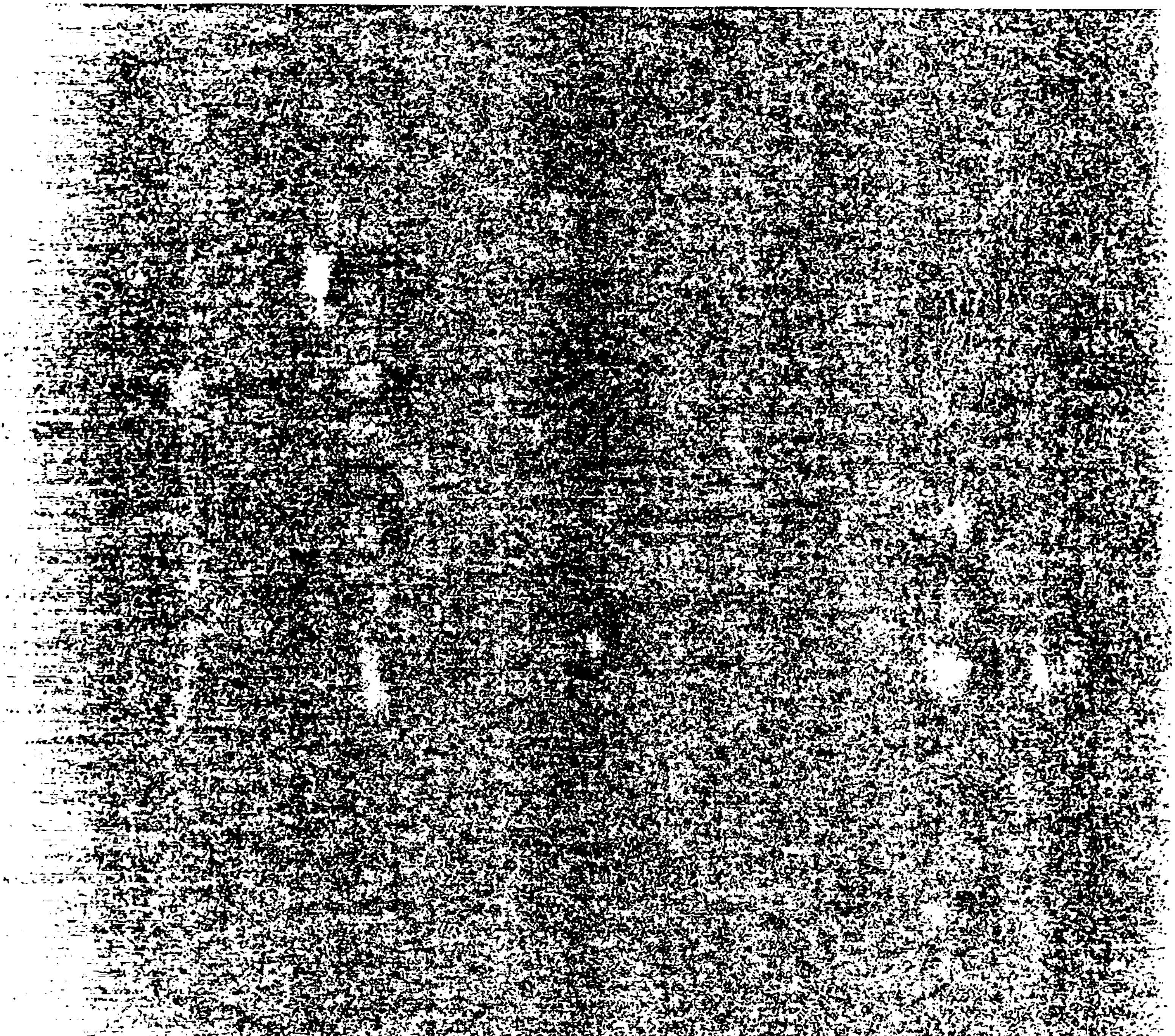

Los Alamos